# SYNTHESIS OF METALLIC PARTICLES WITH ANISOTROPIC MORPHOLOGIES VIA SOLIDIFICATION PATH

A THESIS SUBMITTED TO
THE GRADUATE SCHOOL OF NATURAL AND APPLIED SCIENCES
OF
MIDDLE EAST TECHNICAL UNIVERSITY

BY

MERT ULUSEL

IN PARTIAL FULFILLMENT OF THE REQUIREMENTS
FOR
THE DEGREE OF MASTER OF SCIENCE
IN
METALLURGICAL AND MATERIALS ENGINEERING

AUGUST 2022

Approval of the thesis:

**SYNTHESIS OF METALLIC PARTICLES WITH ANISOTROPIC MORPHOLOGIES VIA SOLIDIFICATION PATH**

submitted by **MERT ULUSEL** in partial fulfillment of the requirements for the degree of **Master of Science in Metallurgical and Materials Engineering Department, Middle East Technical University** by,

Prof. Dr. Halil Kalıpçılar
Dean, Graduate School of **Natural and Applied Sciences** ______________

Prof. Dr. Ali Kalkanlı
Head of Department, **Metallurgical and Materials Engineering** ______________

Assoc. Prof. Dr. Simge Çınar Aygün
Supervisor, **Metallurgical and Materials Engineering, METU** ______________

**Examining Committee Members:**

Prof. Dr. Caner Durucan
Metallurgical and Materials Engineering, METU ______________

Assoc. Prof. Dr. Simge Çınar Aygün
Metallurgical and Materials Engineering, METU ______________

Prof. Dr. Hüsnü Emrah Ünalan
Metallurgical and Materials Engineering, METU ______________

Assoc. Prof. Dr. Emre Büküşoğlu
Chemical Engineering, METU ______________

Assist. Prof. Dr. Recep Yüksel
Chemistry, Eskisehir Osmangazi University ______________

Date:

**I hereby declare that all information in this document has been obtained and presented in accordance with academic rules and ethical conduct. I also declare that, as required by these rules and conduct, I have fully cited and referenced all material and results that are not original to this work.**

Name, Surname: Mert Ulusel

Signature :

# ABSTRACT

## SYNTHESIS OF METALLIC PARTICLES WITH ANISOTROPIC MORPHOLOGIES VIA SOLIDIFICATION PATH

Ulusel, Mert
M.S., Department of Metallurgical and Materials Engineering
Supervisor: Assoc. Prof. Dr. Simge Çınar Aygün

August 2022, 64 pages

The morphology of alloys is dependant on the kinetics and thermodynamics of solidification. While the relation between these phenomena and the microstructure of bulk alloys is known, their effects on particle morphologies has scarcely been studied. Particles are an exceptional model system for the study of nucleation and solidification phenomena because it is possible to isolate individual nucleants, or obtain systems with far less catalytic sites compared to bulk alloys. This makes it possible to obtain undercooling values orders of magnitude greater in comparison to bulk alloys. Large quantities of such particles can be produced with simple physical methods. The potency and distribution of catalytic sites, while not directly observable, can be modified with large scale treatments on particles, making it possible to control the stochasticity associated with the aforementioned events. Distinct particle morphologies, such as Janus particles, the production of which are nontrivial with bottom up methods, can be produced by this approach. In this thesis, by the modification of the solidification parameters, including thermal history, oxygen content of the environment and cooling rate, particles with Janus, Triblock Janus and other distinct morphologies are produced. While the underlying mechanisms are complex, such particles are consistently obtained in the gram scale. Production of even more complex anisotropic morphologies, and the realisation of applications requiring a large amount of such particles are made possible with a top-down approach to particle design.

Keywords: anisotropic particles, janus particles, solidification of liquid alloys, eutectic bismuth-tin

# ÖZ

## KATILAŞMA YÖNTEMİ İLE ANİZOTROPİK MORFOLOJİDE METALİK PARÇACIK SENTEZİ

Ulusel, Mert
Yüksek Lisans, Metalurji ve Malzeme Mühendisliği Bölümü
Tez Yöneticisi: Doç. Dr. Simge Çınar Aygün

Ağustos 2022 , 64 sayfa

Alaşımların morfolojisi, katılaşmanın kinetiğine ve termodinamiğine bağlıdır. Bu fenomenler ile büyük ölçekte üretilen alaşımların mikro yapısı arasındaki ilişki biliniyor olsa da, parçacık morfolojileri üzerindeki etkileri çok az çalışılmıştır. Parçacıklar, çekirdeklenme ve katılaşma olaylarının incelenmesi için iyi bir model sistemdir çünkü bireysel çekirdeklenme bölgelerini izole etmek veya büyük ölçekte üretilen alaşımlara kıyasla çok daha az katalitik bölgeye sahip parçacıklar elde etmek mümkündür. Bu, çok büyük aşırı soğuma değerleri elde etmeyi mümkün kılar. Bu tür parçacıklar, basit fiziksel yöntemler kullanılarak büyük ölçekte üretilebilir. Katalitik bölgelerin gücü ve dağılımı doğrudan gözlemlenebilir olmasa da, parçacıklar üzerinde büyük ölçekli işlemlerle modifiye edilebilir, bu da katılaşma olayının kontrollü gerçekleştirilmesini mümkün kılar. Aşağıdan yukarıya yöntemlerle üretimi zor olan Janus parçacıkları gibi farklı parçacık morfolojileri bu yaklaşımla üretilebilir. Bu tezde, termal geçmiş, ortamın oksijen içeriği ve soğutma hızı gibi katılaşma parametrelerinin modifikasyonu ile Janus ve diğer farklı simetrik olmayan morfolojilere sahip parçacıklar üretilmiştir. Bu tür parçacıklar tutarlı bir şekilde gram ölçeğinde elde edilmiştir. Daha da karmaşık anizotropik morfolojilerin üretimi ve büyük miktarda bu tür parçacık gerektiren uygulamalar, parçacık tasarımına yukarıdan aşağıya bir yaklaşımla mümkün kılınabilir.

Anahtar Kelimeler: anizotropik parçacıklar, janus parçacıkları, sıvı alaşımların katılaşması, ötektik bizmut-kalay

Dedicated to My Family

# ACKNOWLEDGMENTS

Firstly, I would like to express my gratitude to my advisor Assoc. Dr. Simge Çınar for her guidance, her endless patience with me and all the things I learned from her throughout the years.

I would like to thank my thesis committee: Prof. Dr. Caner Durucan, Assoc. Prof. Dr. Emre Büküşoğlu, Prof. Dr. Recep Yüksel and Prof. Dr. Hüsnü Emrah Ünalan.

This work was partially supported by TÜBITAK under grants 117C025 and 119M306.

Serkan Yılmaz, Mustafa Güler and Seda Agar deserve special recognition for their assistance with characterization and being available whenever I needed their help.

I would like to thank my colleagues Orçun Dinçer, Elif Coşkun, Yasemin Aşkar and Bayram Yıldız for their help with my studies and their friendship. I couldn't have asked for a better working environment.

I'm deeply indebted to Ozan Şahin, Özgün Yurdakul, Utku Can Tuğutlu and Nasra Sonat Akşit. Without their friendship, this would be a much more difficult endeavor.

Finally, I am extremely grateful to my mother, late father and my brother who always encouraged me to follow my passion and supported me.

# TABLE OF CONTENTS

CHAPTERS

APPENDICES

# LIST OF FIGURES

FIGURES

# LIST OF ABBREVIATIONS

| | |
|---|---|
| DEG | Diethylene Glycol |
| DET | Droplet Emulsion Technique |
| XRD | X-Ray Diffraction |
| SEM | Scanning Electron Microscopy |
| BSE | Back Scatter Electron |
| DSC | Differential Scanning Calorimetry |
| CNT | Classical Nucleation Theory |
| TEM | Transmission Electron Microscopy |
| EDS | Energy-Dispersive X-ray Spectroscopy |
| FIB | Focused Ion Beam |

# CHAPTER 1

# INTRODUCTION

Control of processing parameters to affect the final microstructure, and thus, the properties of alloys is one of the basic principles of materials science. By changing the cooling rate, the phase transformation kinetics of alloys can be modified, affecting the final solidified microstructure. An example for such behaviour can be given for carbon steel, where the microstructure includes pearlite, which is a phase mixture of cementite and ferrite [1]. The distance between the lamellae consisting of these phases can be decreased by cooling the austenite phase from which they originate with different rates, modifying the mechanical properties of the alloy [2]. The modification of thermal history of alloys is another parameter, control of which is a common method for achieving high strength lightweight aluminium-copper alloys. Off-equilibrium microstructures with fine particles can be obtained by precipitation from super-saturated solid solutions, resulting in strength values otherwise unachievable in the system [3].

In contrast to bulk materials, in the nano-scale, different mechanisms are present. The decrease of the free energy cost of phase separation at this scale may result in complete miscibility of components with limited solubility in each other in the bulk scale [4]. The high ratio of surface atoms to total atoms also results in a melting point depression with decreasing size in particles of this size [5]. These effects open a new area of research, where principles of bulk phase transformations are no longer applicable to predict solidified structures.

However, in the size range of sub-microns, bulk scale mechanisms can be applied in order to produce particles with predictable and controllable microstructures. Among these particle designs, “patchy”, or anisotropic particles, attract special interest, which combat the design limitations associated with their isotropic counterparts [6, 7, 8]. Consisting of regions with distinct chemical, physical, and electrical properties, the interactions of these particles with external stimuli is strongly directional [9]. Janus particles are a special case, owing their name to the two-faced roman god, where the different regions are located at the two hemispheres of the particle. These particles are called core-shell if they consist of a homogeneous core and distinct surface, and coreless, or compartmentalized, if they are chemically homogeneous throughout [10]. The proposed applications for these particles include usage as sensors [11], surfactants [12], micromotors [13] and supramolecular structures [14].

Most existing methods for production of patchy particles are bottom-up, and many involve coatings [15]. One such method is deposition of a metal on homogeneous particles on a substrate [16]. Even though well-defined anisotropic particles can be produced with these methods, their main limitation is yield, preventing enough from being produced in order to realize the aforementioned applications.

In this thesis, large scale fabrication of anisotropic particles was realized by means of fabrication of highly undercooled eutectic bismuth tin particles using droplet emulsion technique (DET) [17] in order to obtain homogeneous particles and reduce variation. Processes analogous to basic processes for alloys in materials science were designed to investigate the relationship between purity, undercooling degree and morphology to obtain sub-micron particles with consistent and distinct morphologies, utilizing the basic principles of solidification.

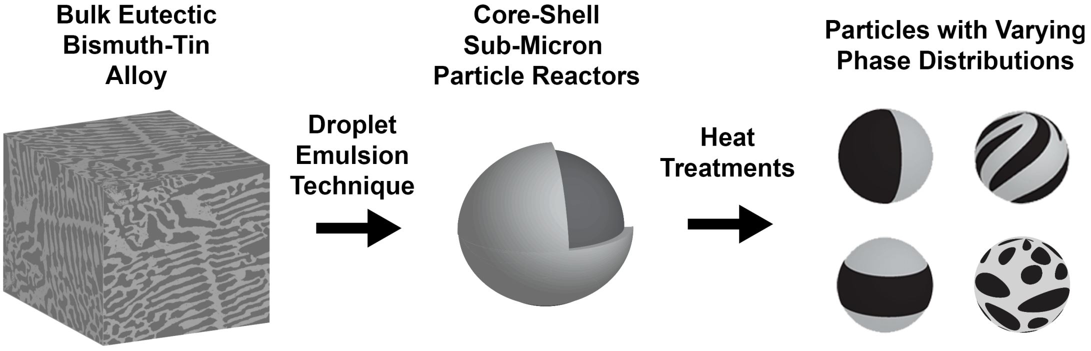

Figure 1.1: Schematic representation of particle reactor production from bulk alloy, and subsequent heat treatments to obtain particles with various phase distributions

# CHAPTER 2

# LITERATURE REVIEW

Anisotropic particles are obtained via altering their solidification behavior in this thesis, thus, to better understand the principles that apply, solidification phenomena and related concepts are first introduced.

## 2.1 Fundamental Concepts

### 2.1.1 Kinetics of Solidification

When a liquid is taken below its equilibrium solidification temperature ($T_m$), spontaneous solidification does not occur in all cases as one might expect. If this liquid phase is metastable, relaxation occurs by nucleation, whereas unstable systems relax by spinodal decomposition [18]. The change from metastable phase to stable phase requires the formation of an interface, which is the basis of the energy barrier associated with nucleation. While initially developed for supercooled vapor condensation into droplets by Volmer and Weber [19], the Classical Nucleation Theory (CNT) has been extended to crystallization of supercooled liquids [20, 21].

#### 2.1.1.1 Homogeneous Nucleation

According to CNT, the free energy change for the formation of a spherical nuclei for liquid to solid phase transition is given by equation 2.1.

$$\Delta G = \frac{4\pi r^3}{3}\Delta G_V + 4\pi r^2 \gamma_{SL} \tag{2.1}$$

where ΔG is the free energy change associated with nucleus formation, r is the radius of nuclei, $\Delta G_V$ is the free energy change per unit volume of phase transformation and $\gamma_{SL}$ is the interfacial energy between the solid and liquid phases. From figure 2.1, it can be seen that as the radius increases, ΔG reaches a local maxima at $r^*$ (the critical nucleus size). The addition of new atoms after this $\Delta G^*$ value results in reduction of the Gibbs free energy, thus this value is the energy barrier associated with nucleation [22].

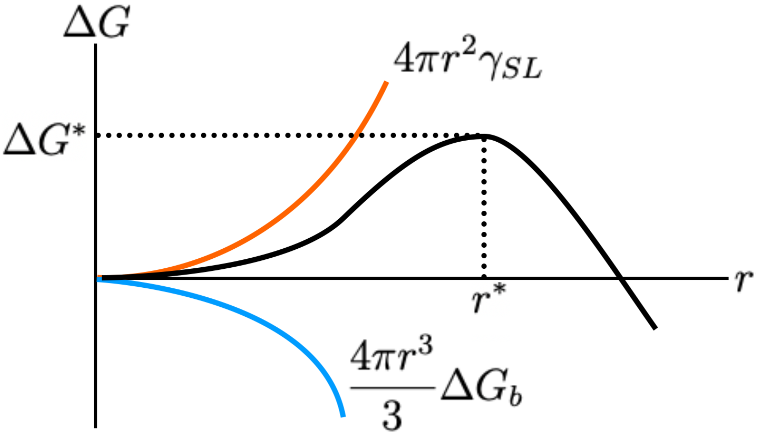

Figure 2.1: The Gibbs free energy of formation of new nuclei with increasing nuclei radius

$\Delta G^*$ can be calculated, by differentiating ΔG with respect to r to find $r^*$, then finding $\Delta G(r^*)$ (equation 2.2).

$$\Delta G^* = \frac{16\pi\gamma_{SL}^3}{3\Delta G_V^2} \tag{2.2}$$

Assuming that any cluster of atoms with a size smaller than $r^*$ will shrink, and larger than $r^*$ will grow, Volmer and Weber formulated the steady state nucleation rate, considering the equilibrium distribution of clusters at temperature T, as seen in equation 2.3 [19].

$$n^* = n_1 exp\left(-\frac{\Delta G}{kT}\right) \tag{2.3}$$

Although the initial stage of nucleation is the most important stage, this steady state solution can also be expanded to cover the dependancy of nucleation rate on time [23]. Thermodynamic, kinetic and experimental data over a wide enough temperature range are not available for most materials. Nucleation rates calculated with CNT assuming homogeneous nucleation fit well with experimental data for silicate glasses shown in figure 2.2a, with a possible cause for the variation being the different purities of the samples [24]. Figure 2.2b illustrates the sensitivity of homogeneous nucleation rate to the surface energy between the nucleating and parent phases for lithium disilicate glass. While CNT overestimates the relation, with a small change in surface energy changing the nucleation rate by orders of magnitude, it shows the importance of surface energy on the phenomenon. In practice, most solidification events initiate on preexisting interfaces.

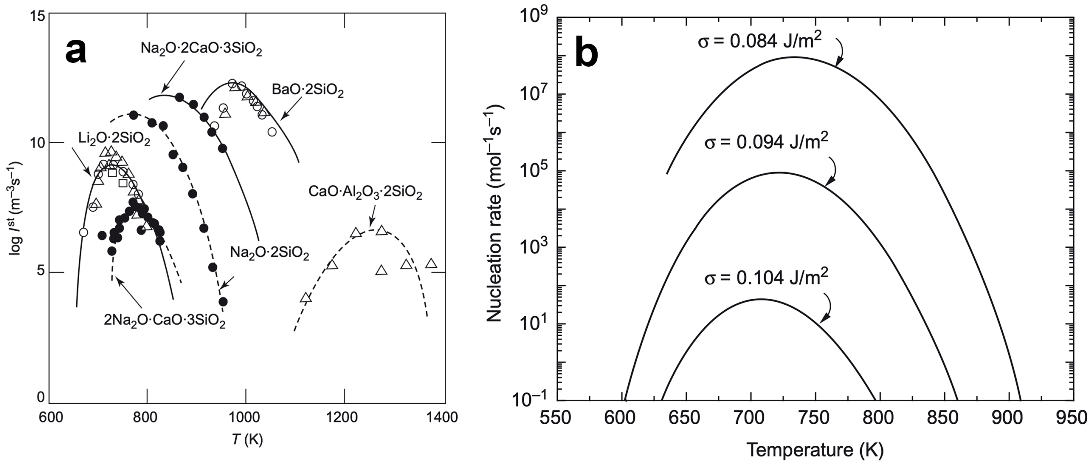

Figure 2.2: a) Measured and calculated dependency of homogeneous nucleation rate of silicate glasses on temperature (Solid lines: Calculated rates for glasses with available thermodynamic data, Points: Experimental data, Dashed lines: Guides for the eye) (retrieved from [24]) b) Dependency of nucleation rate on surface energy (σ: solid-liquid surface energy) (retrieved from [25])

#### 2.1.1.2 Heterogeneous Nucleation

Formation of the nuclei on a preexisting surface reduces the initial energy requirement for surface formation, and thus the energy barrier associated with nucleation [26].

A schematic representation of this condition is illustrated in figure 2.3. Using the

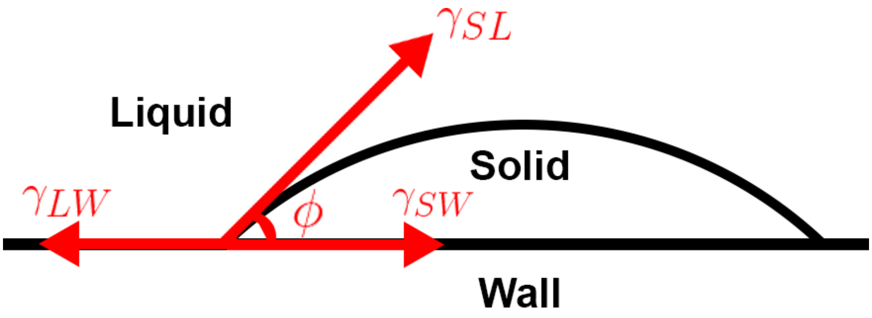

Figure 2.3: Heterogeneous nucleation of the solid phase on a wall, $\phi$ indicates the contact angle between the nucleating phase and the wall, $\gamma$ indicates surface energy

force balance between $\gamma_{SL}$, $\gamma_{LW}$ and $\gamma_{SW}$, and rewriting equation 2.1, the energy barrier for heterogeneous nucleation can be obtained (equation 2.4)

$$\Delta G^*_{het} = \frac{16\pi\gamma^3_{SL}}{3\Delta G^2_V} f(\phi) \tag{2.4}$$

where $f(\phi)$, the catalytic factor, is expressed in equation 2.5.

$$f(\theta) = \frac{2 - 3cos\phi + cos\phi^3}{4} \tag{2.5}$$

With the addition of a single parameter, the contact angle, heterogeneous nucleation can be described by CNT by using the same parameters as homogeneous nucleation [27]. A lower catalytic factor means higher catalytic potency, as with decreasing contact angle, the energy barrier for nucleation also decreases. The contact angle is dependant on both the substrate and the solidifying material, as it is affected by many chemical and physical parameters such as their structure and matching of their lattice parameters [25]. As such, the effect of certain impurities on the the energy barrier, and thus nucleation rate, varies greatly from system to system.

The variation of $f(\phi)$ with changing contact angle is given in figure 2.4. It is clear that any contact angle below 180° is enough to lower the energy barrier, subsequently increasing nucleation rate according to equation 2.3. It is hard to directly measure $\phi$, thus these values are calculated from experimental observations of undercooling values for a given system [28]. However, because CNT has several limiting assump-

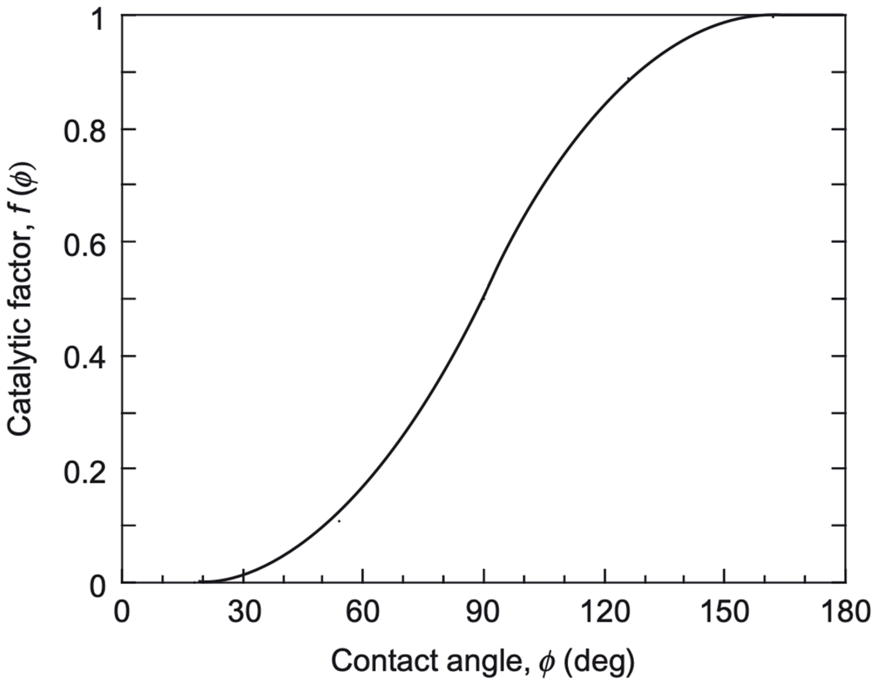

Figure 2.4: Variation of the catalytic factor with changing contact angle

tions, such as the assumption of a sharp boundary between the phases, and not taking into consideration the change in properties of the comparatively small nuclei with respect to macro scale materials, it often fails to quantitatively predict experimental outcomes. Still, it captures the fundamentals of solidification well, and thus is used to qualitatively describe the phenomenon [22]. Figure 2.2b can also be used to illustrate the drastic effect of catalytic potency on nucleation rate, as catalytic factor has the same effect as decreasing surface energy. From this, the importance of the type of catalytic site on the degree of undercooling is clear.

There is a clear preference towards heterogeneous nucleation due to the reduction of the energy barrier. As such, most industrial scale solidification processes initiate with heterogeneous nucleation, the catalysts of which are distributed randomly inside the sample [30]. In addition, the formation of a critical sized nucleus is a stochastic process, with nucleation times being distributed statistically even when repeating the same experiments [31]. There is a strong correlation between solidification kinetics and microstructure. In figure 2.5, the microstructure of Ni65Cu35 alloys undercooled to different degrees can be seen [29]. It is clear that with increasing undercooling, the different phase regions get finer. However, because of the distribution of nucleation

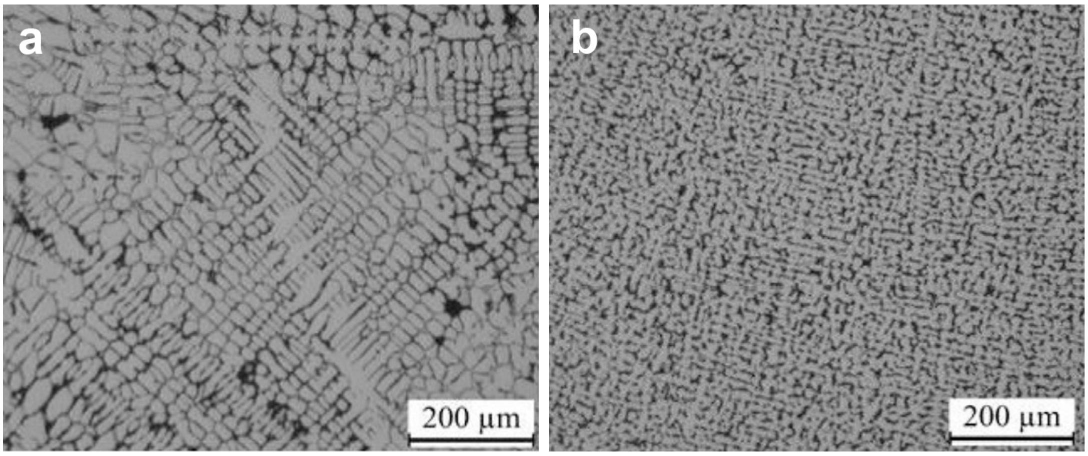

Figure 2.5: Microstructures of Ni65Cu35 alloys undercooled by a) 45 K b) 121 K (retrieved from [29])

sites and nucleation times, there is always some variation in the solidified microstructures. In order to obtain consistent morphologies across particles, the stochasticity associated with solidification needs to be reduced.

## 2.2 Highly Undercooled Particles

The dependence of nucleation rate on catalytic potency of impurities has been established, and their variation contributes to the variation in microstructures by modifying the solidification kinetics. Removal of catalytic sites is one way to reduce stochasticity, and while it is non-trivial for bulk alloys, it has been applied to particles to great effect in order to study the fundamentals of solidification. For bulk materials, this can be done by physical or chemical processes [28], including encasing in inorganic glasses to act as a flux or a physical separation of the melt from surfaces using drop tubes or levitation [32] . To produce particles devoid of catalytic sites, Droplet Emulsion Technique (DET) is an effective approach. DET has initially been used by Turnbull for mercury droplets [33], and improved by Perepezko [34]. In this technique, bulk alloys are brought above their melting point inside a carrier fluid with a high boiling temperature and particles are sheared from the bulk by a blade rotating at high speed. In particles produced this way, catalytic sites which initiate nucleation and solidification are contained in a small fraction of particles, allowing for a majority to stay in the liquid phase well below their melting temperature [28]. The increase in undercooling with decreasing size for micron sized particles has been observed for a variety of pure metal droplets previously [33]. The achievable undercooling is then limited by either homogeneous nucleation or the surface coating of the particles for most of the particles. This method can be extended, using molten salts as a carrier fluid in order to produce particles from metals with higher melting points [35], or by the usage of ceramic matrices which do not catalyze the solidification of said metals [36]. The degree of undercooling of particles produced with this method is strongly dependant on the purity of the initial bulk alloy, as a more pure starting material means less particles with impurities at the end of the process. This phenomena has been shown experimentally by Perepezko (figure 2.6a). Near eutectic bismuth-tin particles with sufficient purity can be made to solidify at 1°C (figure 2.6b), as observed by differential scanning calorimetry (DSC) .

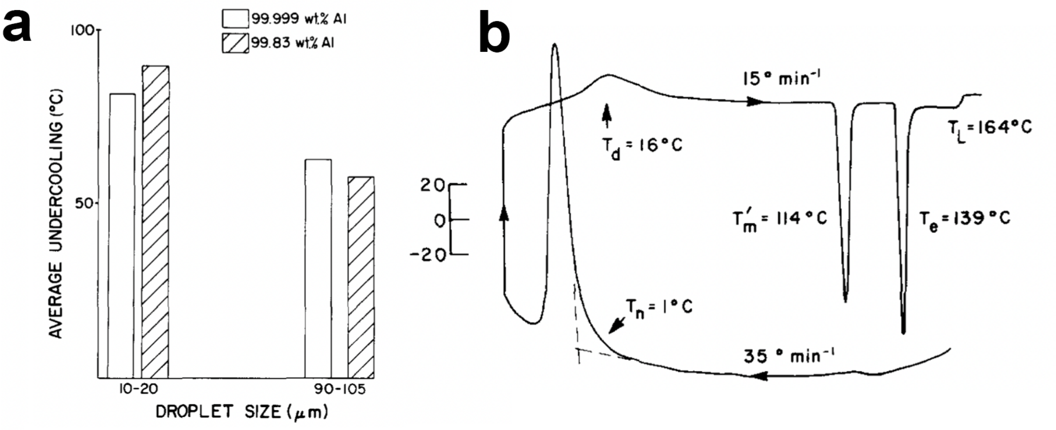

Figure 2.6: a) The dependence of undercooled particle yield on purity of Aluminium b) DSC analysis for Sn-51 at% bi alloy produced by DET (retrieved from [28])

Consistent production of such particles has allowed for direct observation of certain events during solidification. This method allows one to isolate the solidification event taking place at a specific nucleation site. For example, isolation from other sites allows for the observation of the effect of primary phase on catalyzing the solidification of eutectic systems [37]. The behavior of certain nucleating agents in modifying the solidification behavior of highly undercooled particles can also be observed. Perepezko and Wilde studied this effect on pure tin particles with an undercooling of 180°C [38]. Intentionally introduced $Y_2O_3$ particles result in a clear nucleation peak at a specific temperature in addition to the peak corresponding to the nucleation event on the oxide layer. Modification of the oxide layer can also shift the position of this peak to higher temperatures by increasing its catalytic potency. With this method, the catalytic potency of different materials can be compared [37].

In general, high undercooling can have the following features on the solidified phases; refined microstructures, with smaller grain size, increase in solubilities of the constituents in each other, different phase morphologies, and super-saturated or metastable phase formation [34]. For the simple eutectic lead-tin system, for particles in the order of 10-20 microns, a direct relation between undercooling, composition and morphology has been mapped by Chu, Shiohara and Flemings, seen in figure 2.7 [39]. The solidification of the lead-rich phase occurs earlier even for a range of hypoeutectic compositions, causing a shift in the eutectic point 2.7. While the effect of decreasing size on shifting the melting temperature and solubilities of eutectic alloys is known, these effects become prominent in the size range of nanometers [40, 41]. For eutectic bismuth-tin alloy, the calculated undercooling for 10 nanometer particles is 124°C [42], while 138°C undercooling can be achieved for near-eutectic micron sized bismuth-tin particles [28]. The lower solidification temperature is caused by the aforementioned lack of catalytic sites for these micron-sized particles. The reason for the shift in the eutectic points composition, deduced by interrupted DSC and microstructure analysis, is that the oxide layer surrounding the particles is a more effective catalyst for the lead-rich phase. Another significant difference between nanoparticles and emulsified micron sized droplets is that, while the former also melt at a reduced temperature compared to bulk [43], this is not the case for the latter. As the surface effect is not as significant for micron and sub-micron sized particles, the free energy change of melting is still positive at the depressed solidification temperature. Thus, melting is observed around the equilibrium melting temperature [28, 37, 39, 44].

While undercooled particles have been studied extensively, the research is mainly focused on the solidification phenomena itself, and not the produced particles. One exception is the work of Çınar et al., where they used liquid phase Field's metal and bismuth-tin particles produced by DET for heat-free soldering [45]. The control of solidification kinetics allowed by DET opens up opportunities for the engineering of

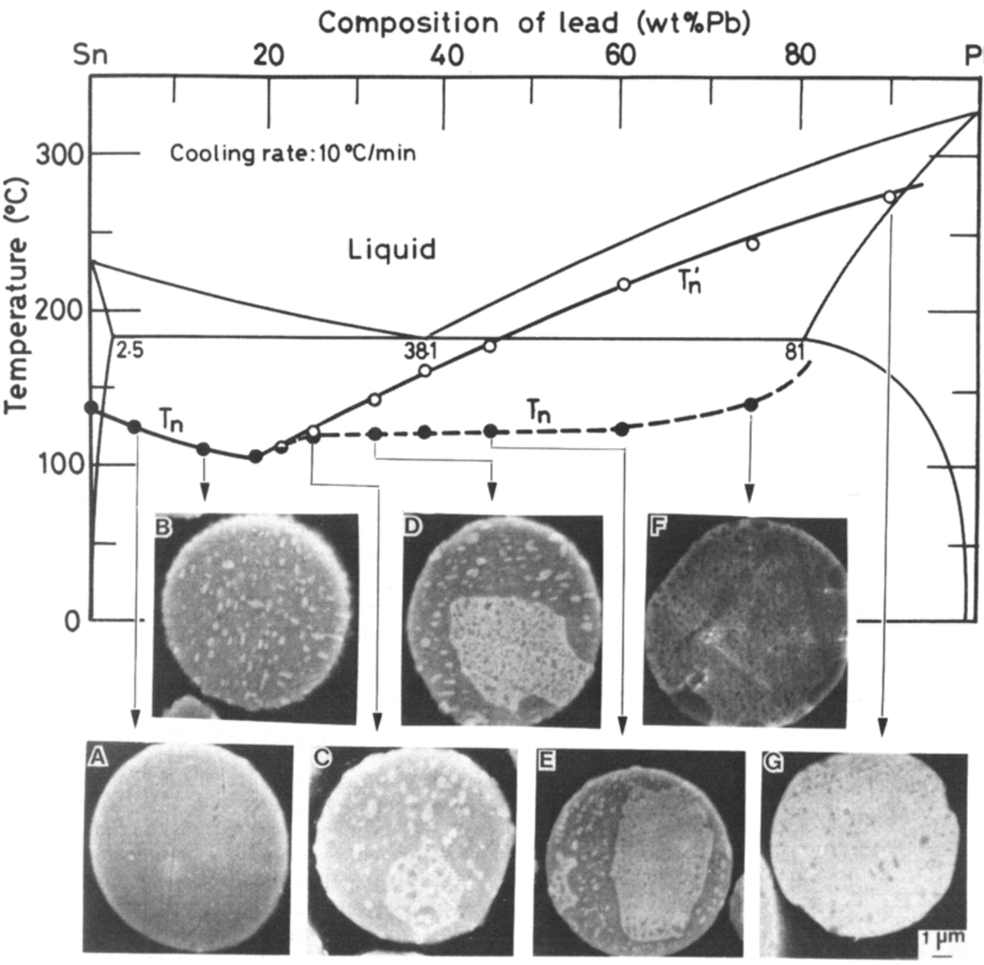

Figure 2.7: The off-equilibrium phase diagram for lead-tin micron sized particles (retrieved from [39])

particles with various structures.

## 2.3 Anisotropic Particles

### 2.3.1 Production Methods

Most of the present methods for the production of Janus particles involve coatings. One such method is the deposition of a metal on homogeneous particles on a substrate, convincingly producing well defined anisotropic particles [13, 46] (figure 2.8a). The amount of particles which can be produced with this process is extremely limited. This two dimensional method can be extended to three dimensions by the usage of emulsions, increasing yield [16]. In a study by Granick et al, an emulsion of water was stabilized by silica particles, and the particles were suspended at the interface by solidifying the wax. The particle-water interface was then functionalized by chemical routes [47] (figure 2.8c). Controlling surface nucleation is another method, resulting in non-spherical Janus particles using a chemical route (figure 2.8d). Another approach, proposed by Lahann et al, utilizes electrohydrodynamic jetting, combined with electrospinning in order to produce Janus cylindrical particles and spheres [48] (figure 2.8f).

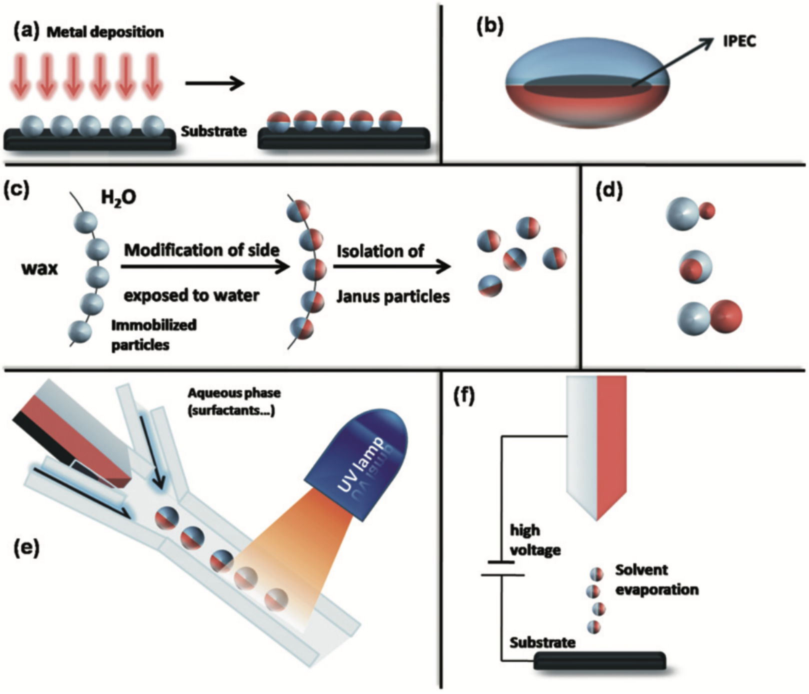

Figure 2.8: Production methods for Janus particles: a) Deposition b) Ellipsoidal complex core coacervate micelle with an interpolyelectrolyte complex core (IPEC) c) Emulsion route d) Controlled surface nucleation e) Microfluidic photopolymerization f) Electrodeposition (retrieved from [16])

Compared to Janus structures, the production of Triblock Janus particles, a.k.a. striped particles, is a greater challenge owing to their more complex structure. For patchy particles, coating methods can be utilized, coating the particles on one side, flipping them over with contact stamping and coating the other side [49], or particle embedding, coating and etching the particle in two steps resulting in a stripe in the center with different surface characteristics [50].

The main limitation of these methods is their low yield, which prevents sufficient amounts of Janus particles to be produced in order to industrialize their application areas. Another disadvantage is that most methods strictly produce core-shell particles, which pose some intrinsic limitations over core-less particles, including degradation over time and swelling. If both chemically and physically homogeneous particles are needed, particle compartmentalization is required [6].

### 2.3.2 Application Areas

Various applications are proposed for such particles, including usage as sensors, surfactants, micromotors and supramolecular structures[51].

Smoukov et al. produced reconfigurable structures with Janus particles consisting of a polystyrene core coated on one hemisphere with iron. Initially disordered, the particles assembled into various structures with the application of a magnetic field. The orientation of the structures could be controlled by rotating the magnetic field. The particles can be demagnetized by application of alternating magnetic fields to disassemble the structures and reconfigured by reapplication of the magnetic field, paving the way for reconfigurable electronics [52]. Amphiphilic Janus particles, consisting of hydrophilic and hydrophobic interfaces, adsorb strongly at interfaces, enabling applications as surfactants. Because such particles can lead to a high reduction in liquid-liquid interface tension in comparison to uniform particles, they can be used as emulsion stabilizing agents [16].

Another proposed application is colloidal motors, which are colloids which exhibit mobility in addition to Brownian motion by using the energy stored in their surroundings. The propulsion can be promoted with chemical reactions as in the cases of self-electrophoresis [53] or bubble propulsion [54]. When Janus particles are suspended an oxidative solution, such as $H_2O_2$ , the oxidation reactions take place on a specific side of the particles due to asymmetry. The resulting asymmetric distribution of ions around the particles generates a local electric field around each particle, resulting in self-electrophoresis, and propulsion. This mechanism can be promoted with the application of light with suitable wavelength [55], generating electron-hole pairs in photo-semiconductors, which then migrate to different parts in the particles and cause the reactions. In systems consisting of particles of sufficient size, the decomposition reaction of the oxidative media can cause bubble formation once the local concentration of oxygen exceeds the solubility limit. These bubbles are ejected with a certain velocity from the particles' surface, transferring their momentum to the particle and causing propulsion. The motion can also be promoted by external power sources, such as electric [56] or magnetic fields [57]. Aforementioned chemical reactions can be induced by electric fields, and rotating magnetic fields can cause rotation, or motion, by continually deforming particles [58].

There are several application areas for colloidal motors. In chemical mechanisms, the velocity of the particles depend on their environment, so by tracking the motion of the particles, information about the medium can also be observed, including the rheology, presence of catalytic ions and pH [59]. Their diffusion can reveal information about the environment, effectively acting as sensors [60]. Another area is cargo carrying for drug delivery applications, by binding specific molecules to the particles and navigating them to specific parts of the body with external stimuli [58].

## 2.4 The Bismuth-Tin System

Bismuth and tin form a eutectic system with a eutectic point at 43 wt% (57 at%) tin, at 139°. Bismuth has a maximum solubility of 21 wt% (13 at%) in tin, while values ranging from 0 to 1 wt% have been reported for the solubility of tin in bismuth [61] (figure 2.9). While pure tin undergoes an allotropic transformation at 13°C, even trace amounts of bismuth is enough to prevent this transformation [62], and so it is not observed in bismuth-tin alloys. The alloy system has widely been investigated as an alternative to lead containing solders [63]. Thorough investigation of the systems mechanical [64] and electrical properties, and the effect of additional alloying elements to the system is still ongoing [65].

Bulk eutectic bismuth-tin alloy has a complex regular microstructure [66]. During solidification of metals, the advancing solid front is characterized by one of two types of interfaces, faceted or non-faceted. For faceted interfaces, there is a strong preference over certain crystallographic orientations, while for non-faceted interfaces, atoms from the liquid phase may attach themselves anywhere on the advancing front. The type of interface is correlated with the entropy of melting of a material, with bismuth growing with a faceted interface and tin with a non-faceted interface. The complex-regular eutectic morphology observed is a result of this mismatch [67]. The types of phase arrangements, as well as the fineness of the individual phases are strongly dependant on cooling rate [68].

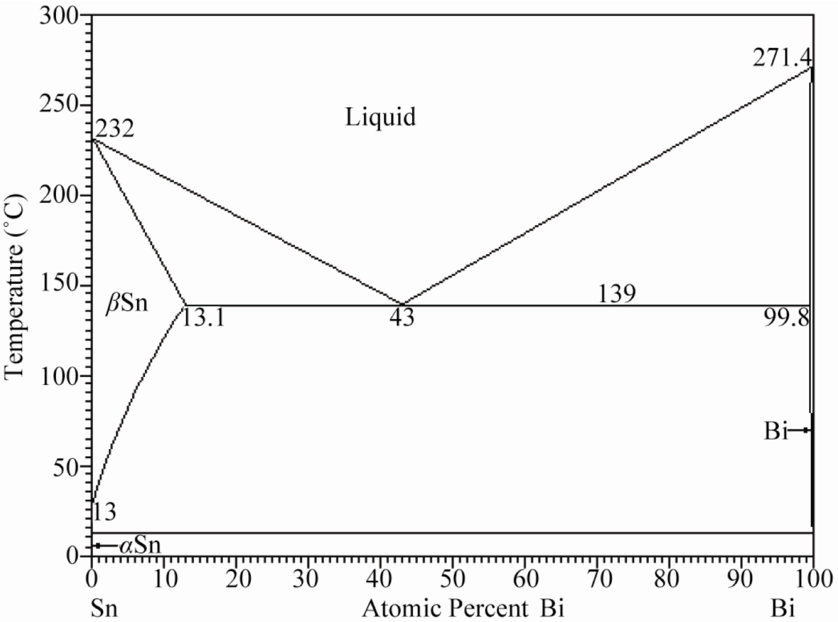

Figure 2.9: The eutectic bismuth-tin phase diagram (retrieved from [69])

### 2.4.1 The Metastable Phases

In alloy systems, more reaction paths during solidification are present compared to pure components, making it possible for numerous metastable phases to develop, including the formation of supersaturated solid solutions [28]. In the literature, there are three metastable phases in bismuth-tin particles, which are BiSn, $Bi_2Sn$ and β', as observed by Pilloni et al. in particles produced by ultrasonication. All of these phases consist of tetragonal tin lattice supersaturated with bismuth to different degrees. The formation of the phases is attributed to the complex environment the alloy melt is exposed to during particle production [70]. In their differential scanning calorimetry analysis, they see a clear endothermic peak at 115°C, which is attributed to the decomposition temperature for the metastable phases 2.10a. The radius of bismuth atoms is larger compared to tin, so the introduction of bismuth atoms to the tin lattice results in an increase in the average inter-atomic separation. Thus, the XRD patterns of the metastable phases matches the pattern of the tin phase (figure 2.10b), shifting towards lower angles because of the increase interplanar distances according to Bragg's law [71].

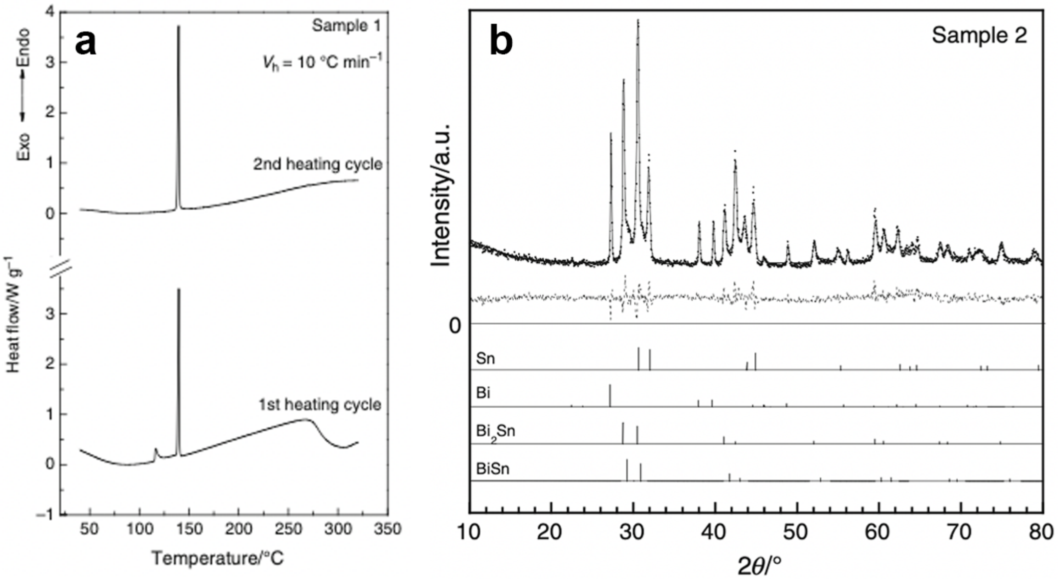

Figure 2.10: a) DSC analysis of eutectic bismuth-tin particles b) XRD pattern of eutectic bismuth-tin particles (Dots: experimental data, solid line: calculated data, dotted lines: the difference profile. Lower vertical bars: reflection positions of Bi, Sn, $Bi_2Sn$ and BiSn phases) (retrieved from [70])

The phases were observed to form under high hydrostatic pressures, and change the morphology of the bismuth-tin eutectic, which was observed as a fine two-phase mixture by Yoon & Perepezko [72]. Bhattacharya et al. also observed the formation of the phase under hydrostatic forces in eutectic bismuth-tin particles embedded in an aluminium matrix. The particles experience pressure due to the expansion of bismuth upon solidification, and the off-equilibrium phases consistently form upon solidification and decompose upon melting [73].

### 2.4.2 Bismuth-Tin Particles

Highly undercooled bismuth-tin particles have been produced in the literature. For particles produced with DET, undercooling degrees of up to 138°C have been observed (figure 2.6).

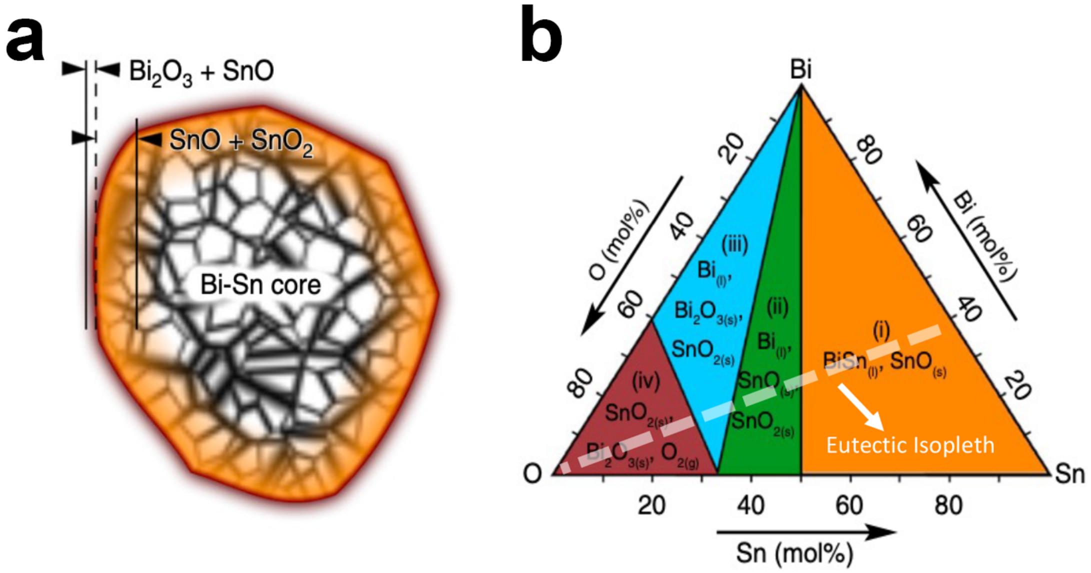

Figure 2.11: a) Heterostructure of eutectic bismuth-tin particles produced by ultrasonication b) Bismuth-Tin-Oxygen ternary phase diagram Dashed line: eutectic bismuth-tin isopleth (retrieved from [74])

Tang et al. produced nanoscale bismuth-tin particles at various compositions for catalysis applications using ultrasonication [74] which has a similar working principle to DET, shearing particles with sonication rather than rotating blades [75]. They characterized the surface of eutectic particles extensively by transmission electron microscopy (TEM) and thermodynamic calculations, modeling the surface and core structure of the nanoparticles (figure 2.11a). For bismuth-tin-oxygen ternary at the eutectic isopleth at 300°C, the most stable oxide phase is SnO, or stannous oxide, until very high oxygen concentration. Thus, Tang et al. concluded that eutectic bismuth-tin nanoparticles' surfaces consists of SnO with traces of $SnO_2$ and $Bi_2O_3$. In the literature liquid tin has been used to produce 2D ultrathin $SnO_x$ by utilizing the spontaneous oxidation characteristic [76], which also allows for mechanically stable particles to be produced from bismuth-tin alloys.

While its low melting temperature and oxidation behavior make this system an excellent candidate for droplet emulsion method, the eutectic composition being close to about half of each component enables close to symmetrical Janus particles to be fabricated at the eutectic composition.

In the literature, the discussed fundamentals have been used to study solidification phenomena and parameters affecting it, such as specific catalytic sites, content of the atmosphere, cooling rate and alloy concentration. Different particles with different morphologies are obtained in this thesis by using highly undercooled particles produced by DET as core-shell reactors, and applying large scale processes to modify the aforementioned parameters. The effect of those parameters on undercooling, and subsequently on the solidified morphology of particles are discovered.

In chapter 3, methods for the synthesis, solidification and subsequent characterization of the particles are outlined.

In chapter 4, solidification of particles devoid of catalytic sites is studied. Fine morphologies resultant from their high undercooling are obtained and characterized.

In chapter 5, the change in solidification behavior due to intentional introduction of catalytic sites and alteration of composition is studied to produce low undercooling particles. Janus and Tri-block Janus particles, for which no bottom-up methods exist in the literature, are produced in large scale and characterized.

# CHAPTER 3

# MATERIALS AND METHODS

## 3.1 Fabrication of Particles

### 3.1.1 Alloy Production

The particles were synthesized from Eutectic Bismuth-Tin alloy (Sn - 57 wt% Bi). Eutectic BiSn alloy was produced from high purity (>99.99%) bismuth and tin metals. Pure bismuth was crushed with a mortar. Elemental tin was cut into the smaller pieces using Abrasive Cutter. Sufficient amounts of both metals were placed in an alumina crucible and, to reduce oxidation, the crucible was filled with silicone oil (Epsilon Kimya). The metal mix was heated to 230°C in the furnace, and the alloy melt was mixed with a glass rod every 45 minutes to ensure homogeneity. After 2 hours, the alloy was air cooled to room temperature.

### 3.1.2 Droplet Emulsion Technique

For the Droplet Emulsion Technique (DET), a Tefal Ultrablend modified with a heat jacket and insulation was used [45] (figure 3.1). During particle production, the reactor was filled with 200 mL of diethylene glycol (DEG) (99.5% purity) purchased from Tekkim. The heat jacked was wrapped around the glass container and set to 200°C. DEG was stirred at 10,000 RPM to ensure uniform temperature distribution inside the reactor. Temperature of DEG was measured every 3 minutes until it reached 160°C. Once heated, 2 grams of eutectic alloy was placed inside the reactor and held there for 1 minute to ensure complete melting. The reactor was set to 45,000 RPM to apply shear force to the alloy melt for 4.5 minutes. The solution was then air cooled to room temperature, and washed three times with ethanol via centrifugation at 10,000 RPM (figure 3.2a). The particles were stored in ethanol.

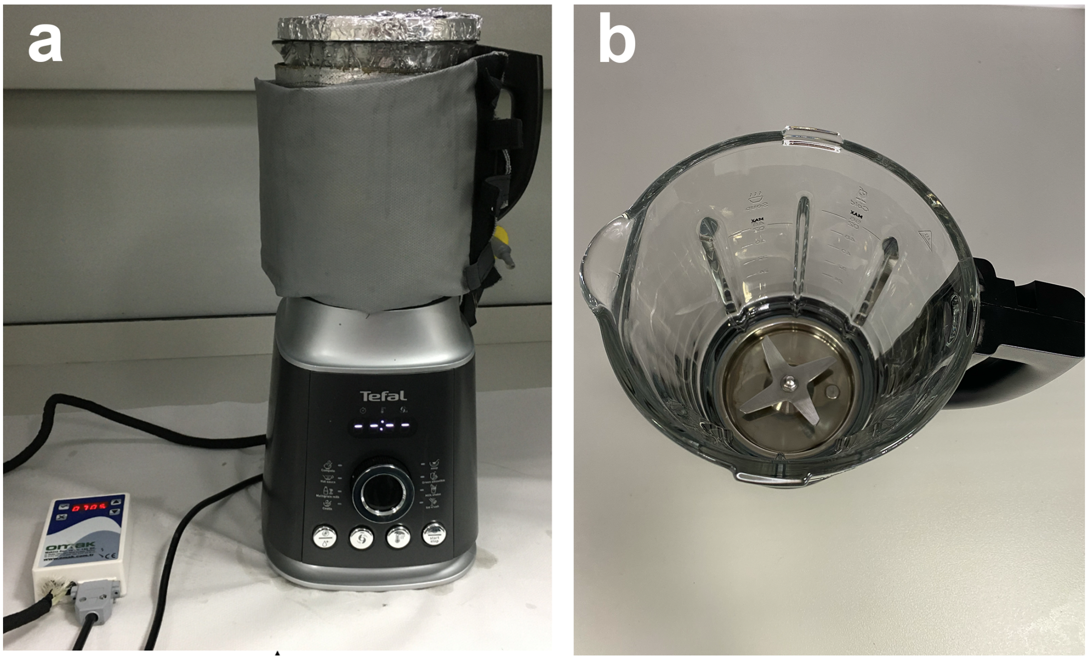

Figure 3.1: The Reactor used for Droplet Emulsion Technique a) modified with a heat jacket b) the blade configuration

Reactor was cleaned prior to production to prevent contamination by impurities, using acetic acid (8 vol%) and ultra pure water. To clean the surface of the alloy, hydrochloric acid (3.5 vol%) was used. The reactor and alloys were cleaned with ethanol.

### 3.1.3 Heat Treatments

The produced particles stored in ethanol were dried on silicon wafers (figure 3.2b). Solidification of particles was done inside a freezer at -20°C for one hour to ensure uniform cooling. Heat treatments were applied in drying oven (Nuve KD 200) at the determined conditions.

To achieve large undercooling solidification, as-produced undercooled particles were directly cooled to -20° inside a freezer, on a silicon wafer for characterization or beaker for large scale production. For solidification with even larger undercooling, as-produced undercooled particles were taken to 160°C, held at that temperature, then furnace cooled to 90°C with 2.5°C/min, and directly quenched to -20°C by placing inside the freezer. To introduce catalytic sites, solidified particles were heated to 160°, held at that temperature in open atmosphere, and furnace cooled with a rate of 2.5°C/min to room temperature. To modify the composition of the eutectic particles, as-produced particles were heated to 230°C inside the drying oven in open atmosphere, held at that temperature, and furnace cooled with 2.5°C/min to room temperature. The heat treatment experiments were repeated for 15 minutes, 1 hour, 6 hours, 24 hours and 48 hours to study the effect of heat treatment time on the final morphology.

To scale up the processes, heat treatments were applied to larger amounts of particles dried inside glassware (figure 3.2c).

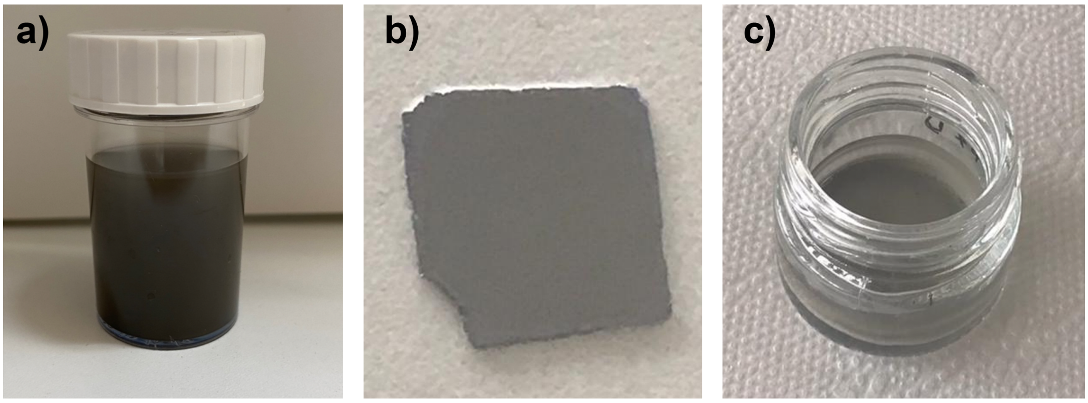

Figure 3.2: a) Particles produced with DET after centrifugation b) Silicon wafer coated with particles for heat treatments, and subsequent SEM and XRD analyses c) Large scale application of the heat treatments to particles inside glassware

## 3.2 Characterization of Particles

Back Scatter Electron Scanning Electron Microscopy (BSE-SEM) analysis and Energy Dispersive Spectroscopy and EDS mapping were done with FEI Nova NanoSEM 430. Particles suspensions inside ethanol were dried on silicon wafers and analyzed.

FIB analyses were done with FEI Nanolab 600I. Particle were first coated with platinum, then milled with 30 kV Ga+.

Transmission electron microscopy (TEM) analyses were done with FEI Tecnai F30. Samples suspended in ethanol were dried on carbon-coated copper TEM grids. To obtain particles smaller than 100 nanometers, particles were centrifuged for 15 minutes at 5000 rpm, supernatant was removed and dried at 60°C to increase the concentration of the solution. Heat treatments were applied to concentrated solutions of particles inside glassware.

XRD analyses were performed with Rigaku DMAX2200, with a step width of 0.02° and scanning rate of 1°/min. Particles measured were dried on single crystal silicon wafers of orientation <4 0 0> in order to prevent noise from the substrate. Multiple droplets of particle suspension were dried on the wafer depending on the concentration of the suspension to ensure the entire wafer was coated with particles, reducing noise from the substrate.

Differential scanning calorimetry analyses were performed with TA instruments DSC250 using aluminum pans in air and nitrogen atmosphere with a cooling rate of 2.5°C/min. 2 mg of particles were used for each experiment. Particles suspended in ethanol were dried on the pans. To analyze the microstructure of DSC samples, the lids of the aluminium pans were removed and directly analyzed under SEM.

# CHAPTER 4

# HIGH UNDERCOOLING MORPHOLOGIES

## 4.1 As-Produced Particles

If the particles are not sufficiently pure, or size refinement is not sufficient, high undercooling will not be observed for particles produced with DET. In figure 4.1a, in the BSE-SEM micrograph of eutectic bismuth-tin particles, large variations in microstructure can be observed. In contrast, a more uniform structure distribution can be achieved by ensuring removal of catalytic sites (figure 4.1b).

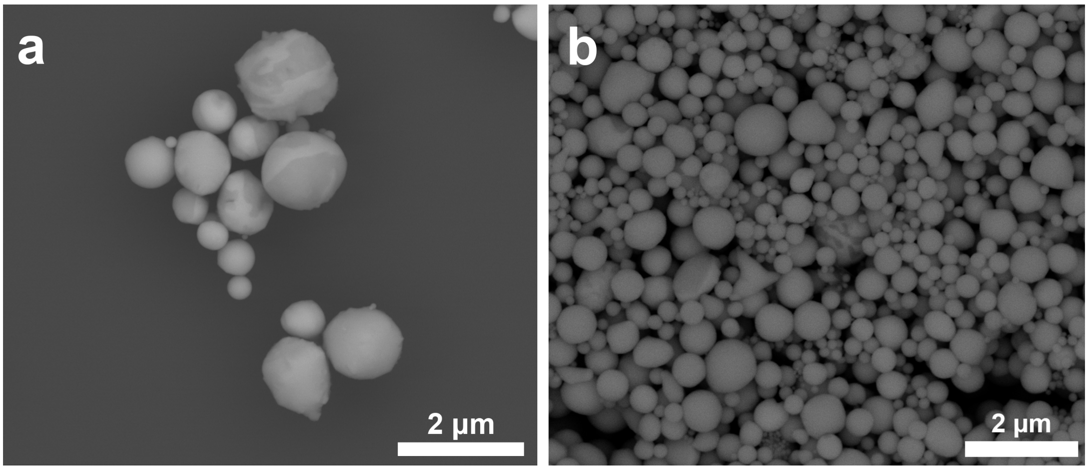

Figure 4.1: a) Randomly solidified eutectic bismuth-tin particles produced with DET b) Undercooled eutectic bismuth-tin particles produced with DET

In the BSE-SEM micrograph of the as-produced particles (figure 4.1b), several phase distribution characteristics are observed across the particles. In BSE-SEM, in addition to secondary electrons which provide topological information, majority of the signal comes from backscattered electrons in which the signal strength is directly correlated with the elements atomic number [77]. As such, because bismuth is partially soluble in tin at room temperature (with a maximum of 21 wt%), and tin is not soluble in bismuth (figure 2.9), one would expect to see two distinct contrast regions corresponding to the pure bismuth and tin-rich regions, as in bulk bismuth tin alloy. However, in a majority of the particles, no contrast is observed, and instead, the particles are uniform throughout, indicating the presence of a single phase, or the metastable liquid in this case (figure 4.2).

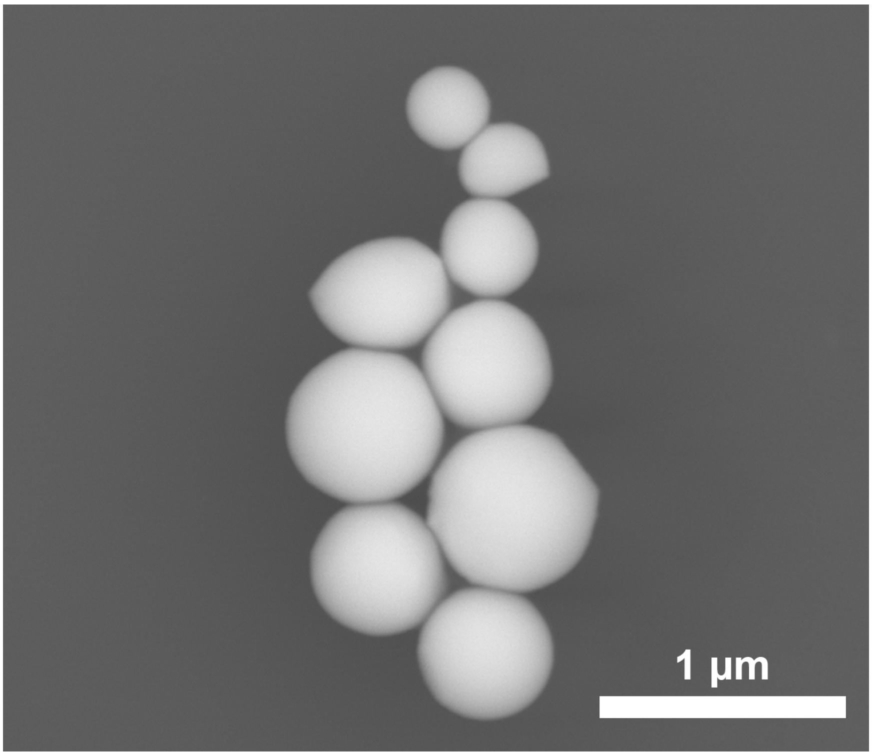

Figure 4.2: BSE-SEM image of undercooled particles

A variety of phases are present in the X-ray Diffraction (XRD) pattern (figure 4.3) of the particles produced with DET. Here, in addition to the equilibrium bismuth and tin solid solution phases of the eutectic system, peaks belonging to additional metastable phases can be observed. Because the inter-atomic separation of pure tin is lower than pure bismuth, the dissolution of bismuth atoms in the tetragonal tin lattice results in an increase in the average distance, and thus a slight shift to lower angles is observed in the tin peaks according to Bragg's law [71].

The first metastable phase is evidenced by the broad peak spanning 25° to 40° in the XRD pattern, indicating the presence of short range order, or an amorphous phase in

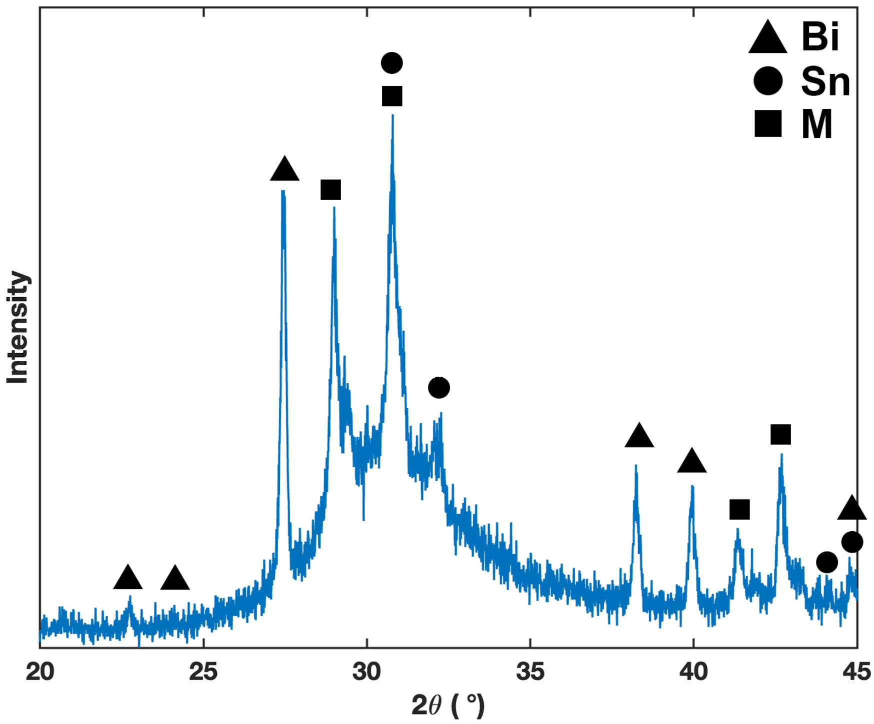

Figure 4.3: XRD pattern of the as-produced eutectic bismuth-tin particles showing bismuth (PDF 04-006-7762), tin (PDF 04-008-4977) and metastable phase peaks (metastable phase peaks retrieved from [70])

the particles' structures. Since diffraction is observed at specific angles corresponding to specific interplanar spacings in crystals with long range order according to Bragg's law, they appear as peaks in the diffraction pattern. However, in amorphous materials, there is a lack of periodicity, so instead of sharp peaks, a broad peak corresponding to the statistical preference of inter-atomic separation of the material is present [71], further proving that the particles are in the liquid phase.

In the Energy-dispersive X-ray spectroscopy (EDS) map of an individual particle without any backscatter contrast (figure 4.4), it is seen that bismuth and tin elements are distributed uniformly throughout the particle. It can be further concluded that in the particles, the elements have fully dissolved in each other at room temperature, as is the case in liquid bismuth-tin, while also indicating that the particles are homogeneous throughout their core.

Heterogeneous nucleation initiating from container walls is a common occurrence [78], which is not observed in the produced particles. In the case of the undercooled

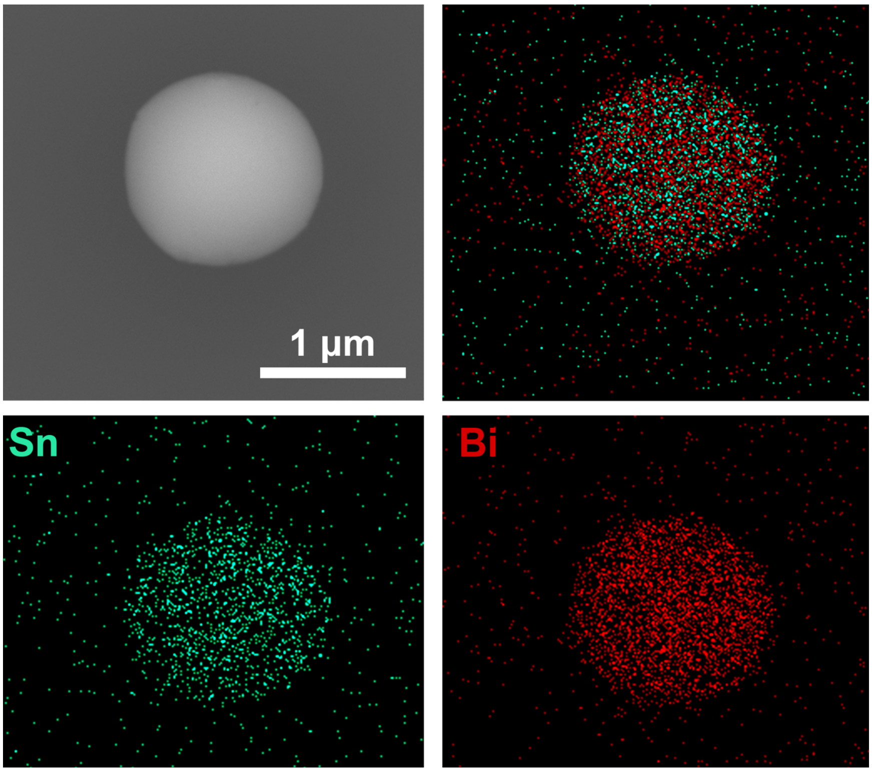

Figure 4.4: The EDS map of an Undercooled particle

particles, they can retain their shape and undercooled characteristic even after centrifugation under up to 15,000 RPM, and retain their metastability for up to three years. During production with DET, as the particles are sheared above their melting point in DEG, their surfaces spontaneously oxidize, forming a thin protective oxide shell [79]. As discussed previously, for eutectic bismuth-tin particles produced by ultrasonication, their surfaces consist mostly of SnO (figure 2.11). This kinetic and mechanical stability, and the fact that no XRD peaks are observed of any oxide phases in the pattern(figure 4.3) leads to the conclusion that the surface of the produced particles consists of an either very thin, or amorphous coating containing various oxides of bismuth and tin, consisting mostly of SnO. The amorphous characteristic of the particles' surfaces is reinforced by the fact that it does not catalyze solidification, as non-crystalline surfaces make for poor catalytic sites for crystal nucleation [28]. These uniform particles with no present catalytic sites have been used as a starting material for the rest of the study.

The particle size distribution is given in figure 4.5. Particles are mostly in the sub-micron range due to the high RPM used while producing them for sufficient refinement, with a monomodal distribution. The particles are in the range of 60 nm and 1.2 microns, with an average particle size of 300 nm. Digital segmentation of 2000 individual particles from SEM micrographs via watershed algorithm, and subsequent measurement of their sizes results in a similar size distribution (Appendix A).

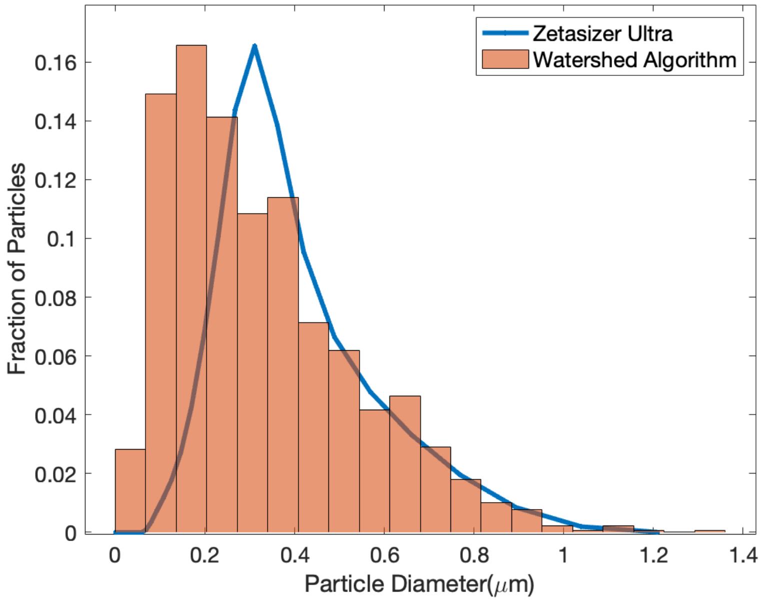

Figure 4.5: Size distribution of the as-produced particles

The second metastable phase shows itself as a third phase region in BSE-SEM micrographs of particles that either solidify during production, or that are solidified with high undercooling, milled by focused ion beam (figure 4.6). In addition to the two regions corresponding to the tin-rich solid solution and bismuth phases, a third region can be observed. This region consists of elements with an average atomic number between the two equilibrium phases, and corresponds to a super-saturated tin lattice. The peaks observed in as-produced particles align with the BiSn and $Bi_2Sn$ peaks reported by Pilloni et al. [70]. The metastable phase is generally attributed to high pressure environments in the literature [72, 73]. Though the pressure is not as high in the DET reactor in this study, the non-equilibrium conditions, such as the constant shear force on the particles, may have aided in the formation of such phases.

In this study, the metastable phases are obtained only as a product of DET, and once

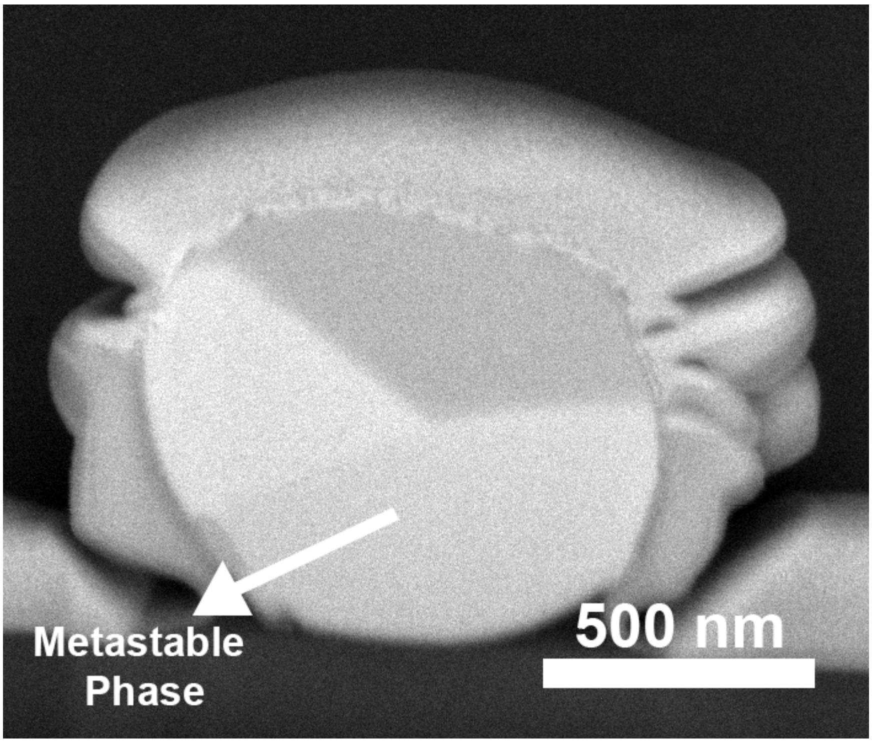

Figure 4.6: BSE-SEM image of an as-produced particles core, milled using FIB

taken and held above their decomposition temperature for a sufficient amount of time, they do not form upon cooling back to room temperature. As such, no correlation between these phases and the various obtained particle morphologies has been drawn.

According to the classical theory of nucleation, nucleation rate is correlated with temperature, as well as the energy barrier of nucleation (equation 2.2) at that specific temperature. The potency of a specific catalytic site relates to the surface energy term in the energy barrier, with a lower surface energy meaning higher catalytic potency. However, from equation 2.3, it is apparent that nucleation is possible for high surface energy sites if the temperature is sufficiently low, i.e. a high enough undercooling is achieved. Another implication of equation 2.3 is that solidification temperature from a given nucleant is characteristic, as for a specific $\gamma_{SL}$ term, nucleation rate is high enough to initiate solidification at a specific temperature.

When the particles are cooled to -80°C, an exothermic peak with an onset temperature of -7°C is observed in differential scanning calorimetry analysis (figure 4.7). When the particles are heated back up to room temperature, no corresponding endothermic

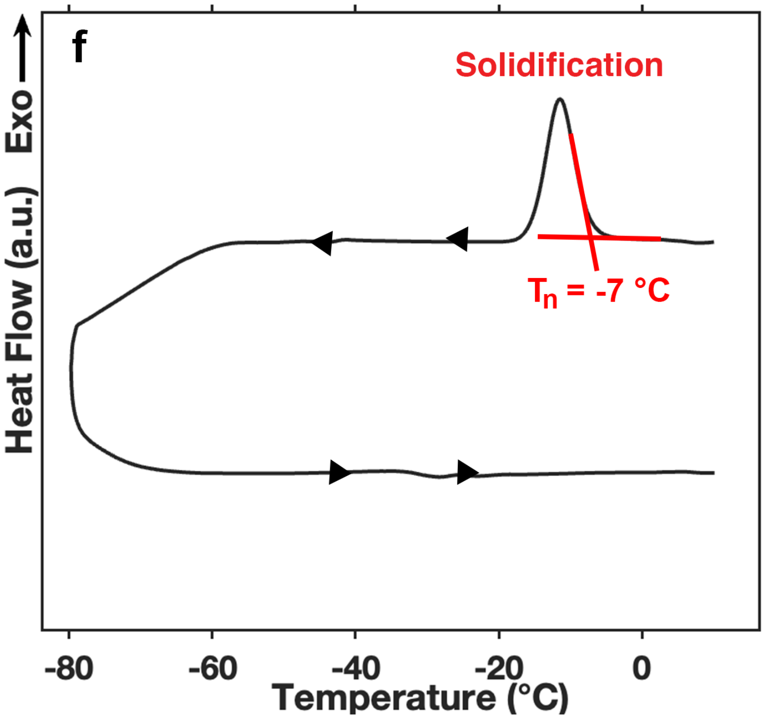

Figure 4.7: DSC analysis of the solidification of highly undercooled as-produced particles

event is observed at the same temperature, leading to the conclusion that this event corresponds to the off-equilibrium solidification of the undercooled particles, further proving their liquid characteristic. As the particles transform to their stable phases, the event is irreversible, and the particles need to be heated up to 139°C to melt them. The common characteristic of the highly undercooled particles is the aforementioned amorphous oxide shell. It is concluded that the solidification event at this temperature initiates from the shell. The shell either acts as a catalytic site, or as the particles are spherical in geometry, when the particles are cooled, the melt at the outermost part reaches the nucleation temperature. Either way, 150°C undercooling is required to solidify the particles. As the event temperature is identified, undercooled particles are treated at -20°C in large scale to ensure solidification for further analysis.

Because there is a direct correlation between the purity of the initial alloy and undercooling degree, extra care has been taken to clean the DET experimental setup and initial alloy in order to decrease impurities and increase the undercooled particle fraction of the synthesized particles. The particles produced this way stay in liquid phase at room temperature for up to three years.

## 4.2 Lamellar Particles

When the metastable undercooled particles are solidified, a distinct but consistent morphology is observed. The undercooled particles have transformed into their equilibrium phases, and the single phase liquid has segregated into two phase regions, apparent in the BSE-SEM image as two distinct contrasts (figure 4.8).

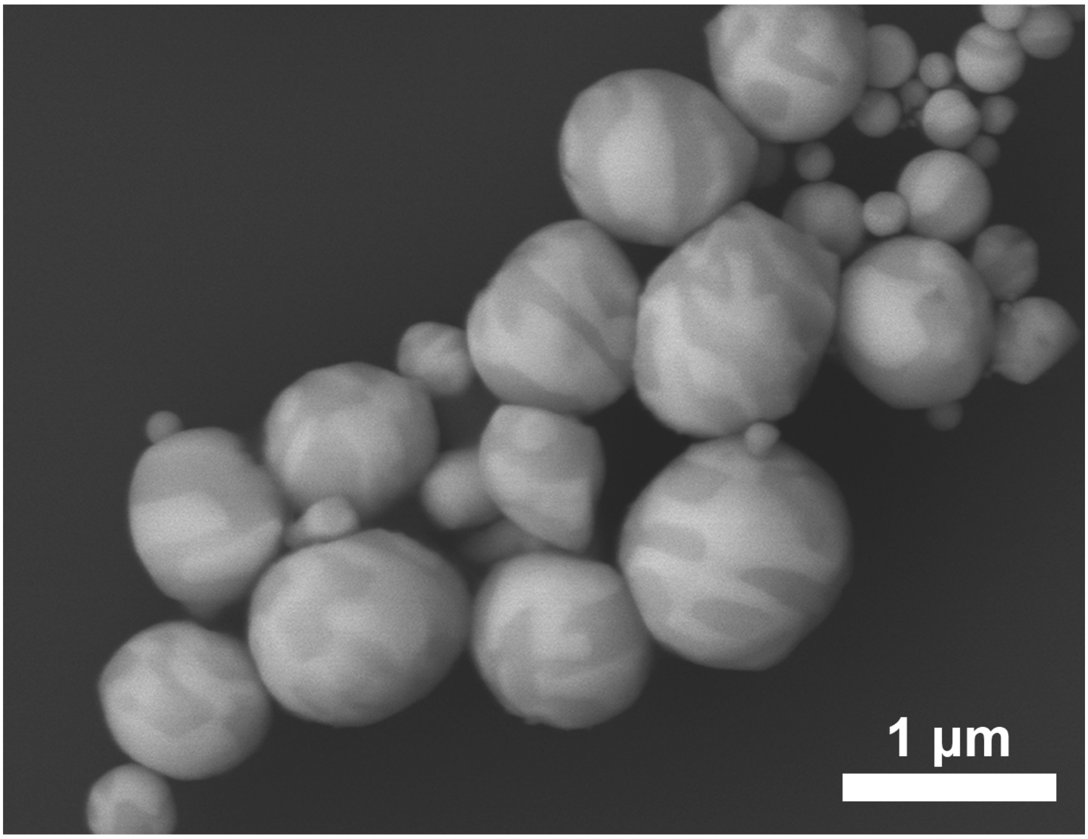

Figure 4.8: BSE-SEM micrograph of the particles solidifed at -7°C

This morphology resembles that of a complex-regular eutectic structure, observed in bulk bismuth tin eutectics. This morphology is named *Lamellar Particles*. One distinctive feature in these particles is the inter-phase spacing between the two equilibrium phase regions (figure 4.9). In the bulk alloy where solidification initiates from a container wall with low undercooling, the interlamellar spacing is in the order of a few micrometers. In comparison, the Lamellar particles were solidified with a much larger undercooling, as the oxide shell from which solidification initiates has a low catalytic potency. Compared to the morphology of similar particles solidified with high undercooling in figure 2.7, where two distinct phase regions are observed inside the particles, Lamellar particles are more homogeneous. A possible explanation might be the fact that the oxide layer surrounding the lead-tin particles is a much more effective catalyst for the lead-rich phase, resulting in the preferential nucleation of this phase at lead concentrations higher than the metastable eutectic temperature. If the bismuth and tin-rich phases of the Lamellar particles show no such preference, a more homogeneous structure is expected. Size refinement might play a role, as the lead-tin particles are a few microns compared to the mostly sub-micron Lamellar particles.

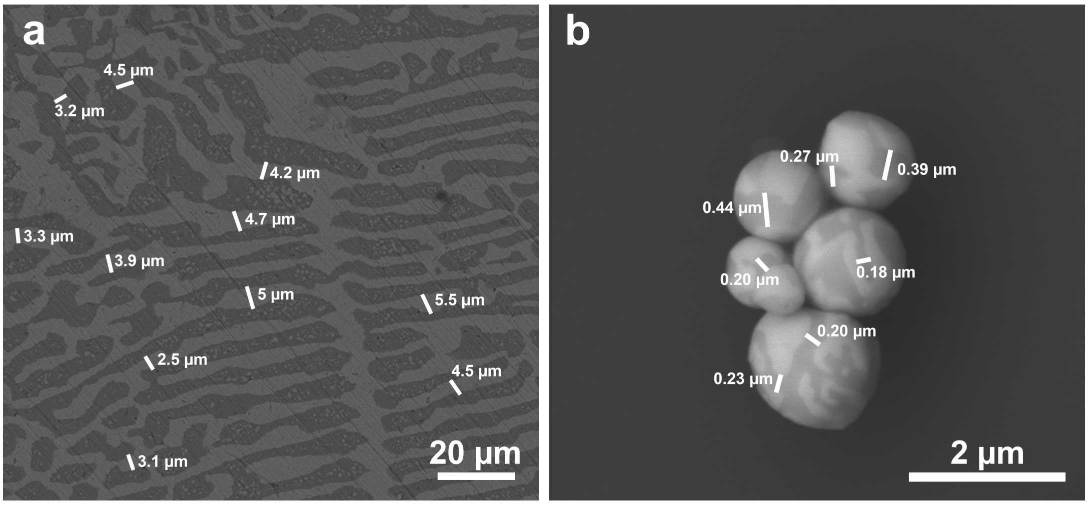

Figure 4.9: BSE-SEM micrographs of a) Bulk eutectic bismuth-tin alloy and b) Lamellar particles, with interphase spacing measurements

For eutectic alloys, there is a relationship between the degree of undercooling and the interlamellar spacing. This relation is also observed in eutectic alloy particles. Han and Wei quantified this relation by using droplets of several hundred micrometers in order to study containerless solidification, and reported a direct correlation between droplet size and interlamellar spacing, as well as an inverse correlation between droplet size and undercooling [80]. This leads to the conclusion that, as undercooling increases, interlamellar spacing decreases in droplets, consistent with the increasing nucleation rate 2.3.

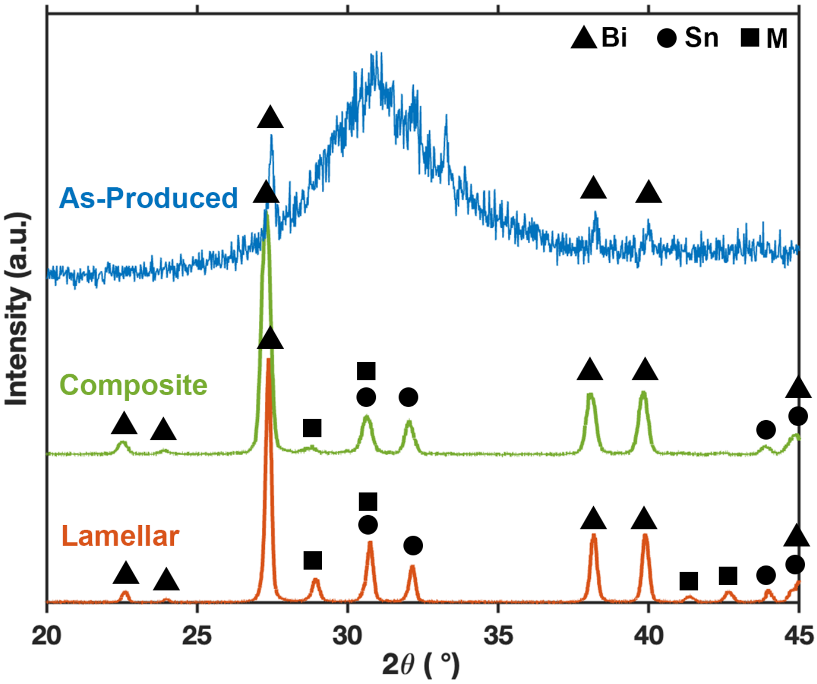

Figure 4.10: XRD pattern of the phase distributions achieved with large undercooling, showing bismuth (PDF 04-006-7762), tin (PDF 04-008-4977) and metastable phase peaks (metastable phase peaks retrieved from [70])

The XRD patterns of all particles with large undercooling phase distributions are plotted in figure 4.10 for a higher undercooled particle yield batch. Much less signal from solid particles is present in comparison to figure 4.3. After solidification of the particles, the large peak disappears, and the crystal phase peaks are more pronounced. As no treatment at high temperature was applied to these particles, the metastable phase peaks are retained. The equilibrium phase peaks are much more intense in comparison, since the batch consisting mostly of undercooled particles have solidified as these phases.

For further analysis, Lamellar particles are milled using FIB to investigate their core structures (figure 4.11). Their core morphology is found to be consistent with their surface morphology, with several hundred nanometer tin lamellae distributed inside the bismuth matrix. As solidification likely initiates from the surface and proceeds across the particle, this consistency is expected.

To analyze the effect of thermal cycling on the as-produced particles, after solid-

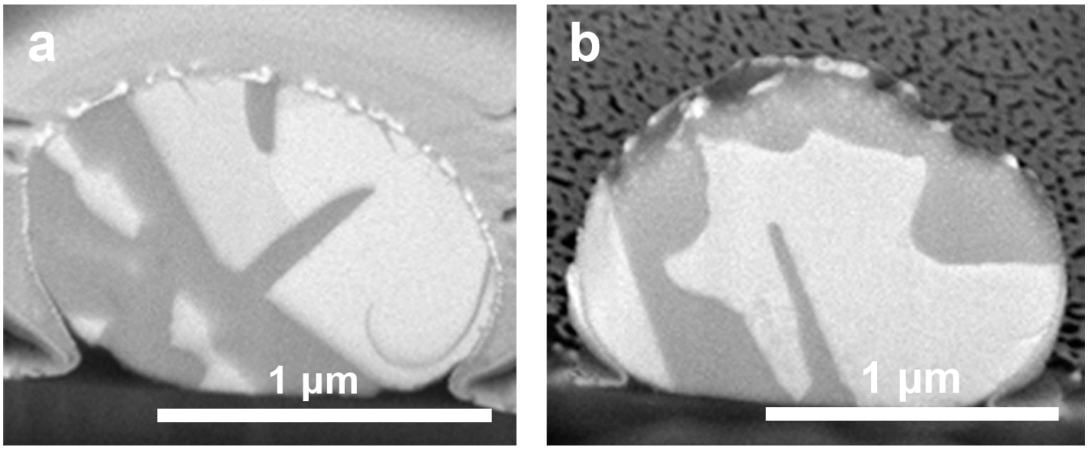

Figure 4.11: BSE-SEM micrographs of Lamellar particles' cores, milled using FIB

ification at -7°C, they were brought above their melting point, and re-solidified at sub-zero temperatures in inert nitrogen atmosphere with a heating rate of 2.5°C/min (figure 4.12). Two endothermic peaks are present at 115°C and 139°. Heating after initial solidification, the metastable phase decomposition occurs at the first endothermic event, and melting occurs at the second event at the eutectic temperature. In the second cooling cycle, two peaks are present, one at onset temperature of 86°C and another with -7°C. Here, the low temperature peak corresponds to the previously discussed solidification from the oxide shell, while the first one indicates another prominent catalytic site in the particles, further discussed in chapter 5.

In comparison to undercooled particles, the solidified particles are less spherical. Tin, like most elements, shrinks upon solidification, while elemental bismuth is more dense in its liquid state compared to solid, and its volume increases by 3.2% upon solidification [81]. This discrepancy might be a reason for the deviation of the solidified particles' shapes from sphericity.

## 4.3 Composite Particles

To obtain finer structures, particles were quenched below their sub-zero solidification temperature to further increase the degree of undercooling. The effect of increasing cooling rate on the nucleation temperature of eutectic bismuth-tin particles can be seen clearly with DSC analysis (figure 4.13).

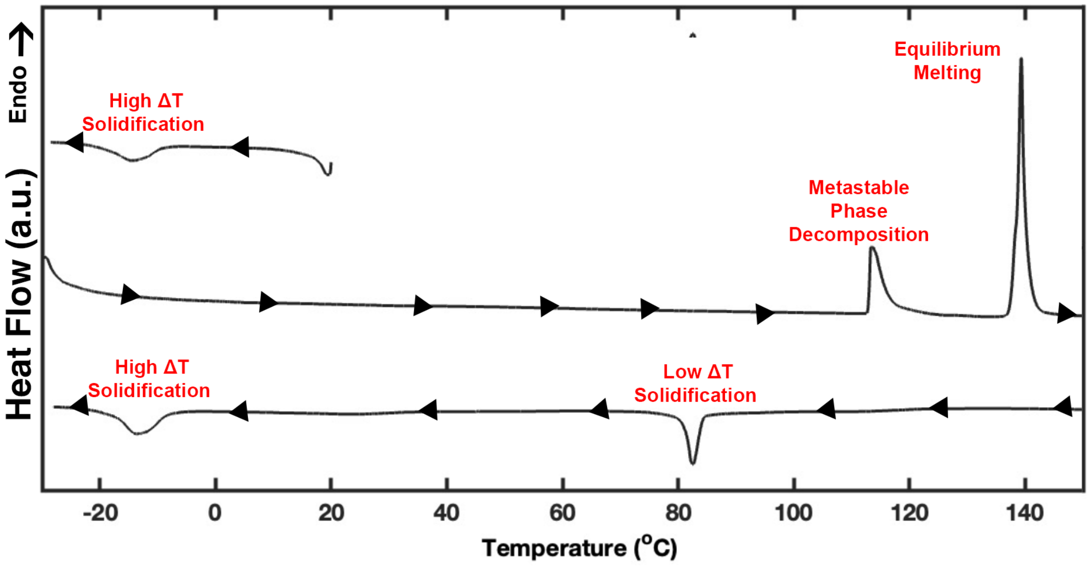

Figure 4.12: DSC analysis of the thermal cycling of as-produced particles under inert nitrogen atmosphere

It is known that generally, a larger cooling rate corresponds to a higher degree of undercooling upon solidification [82]. Although increasing undercooling is known to result in finer lamellar eutectic structures, it is hard to isolate and study the effect of cooling rate on the structure because of the aforementioned relation. Zhai et al. studied the effect of cooling rate on the solidification of eutectic bismuth-tin particles in the size range of 10 to 50 micrometers, and concluded that while there is no direct correlation, both cooling rate and particle size affect the degree of undercooling, which in turn affects the final solidified morphology [83]. The already low solidification temperature can be lowered further by utilizing this, combining the undercooling degree from lack of catalytic sites with cooling rate.

To observe the effect of this shift on the phase distribution of the particles, this process was applied in the bulk scale to undercooled particles, heating them up to 160°C, holding them at this temperature for 6 hours and quenching them from 90°C to -20°C. This temperature was chosen to quench the particles from above both the high and low catalytic potency site initiated nucleation events. As a result, another distinct morphology is observed. In these particles, instead of interconnected networks of tin-rich phase lamellae, the tin phase is distributed as small regions resembling precipitates inside a matrix, they were thus labelled *"Composite Particles"* (figure 4.14).

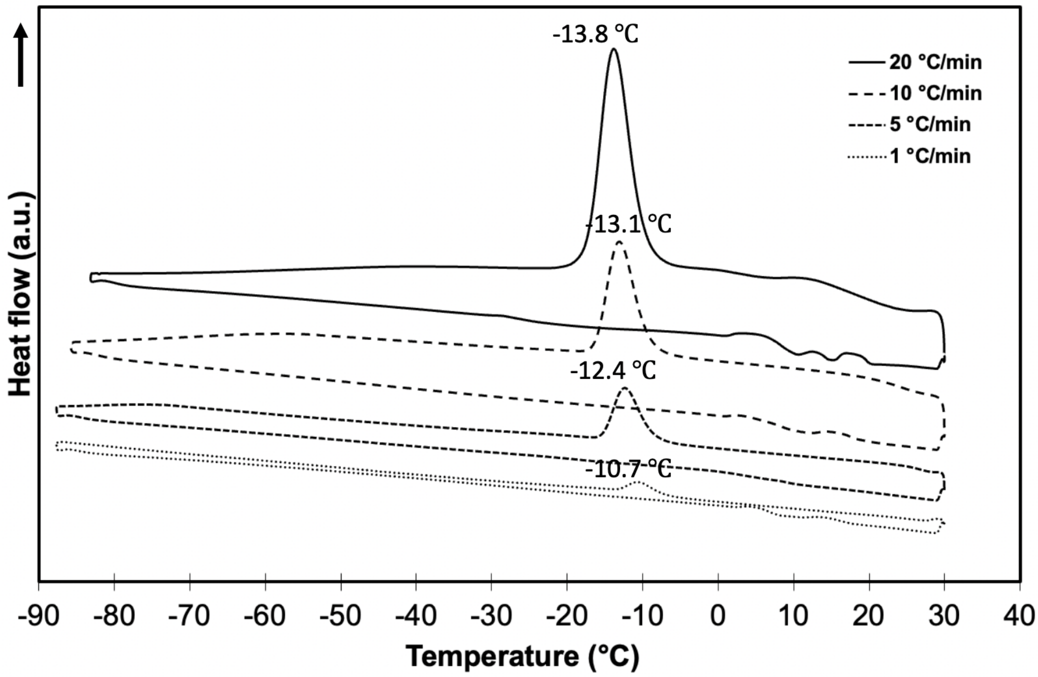

Figure 4.13: DSC analysis of the effect of cooling rate on the solidification peak position of as-produced particles

In comparison to Lamellar particles, the interface area between the two phases is much larger. This shift of morphology in eutectics with higher undercooling has been reported in the literature for particles [80], and in this case, is attributed to the higher nucleation rate and lower growth rate at lower temperatures. Although the exact cooling rate is not quantified, from the resultant phase distributions, it is apparent that this treatment has an effect on the solidification kinetics.

This shift in solidification kinetics is more apparent when the cores of the Composite particles, milled with FIB, are observed (figure 4.15). In comparison to Lamellar particles, more disconnected regions of tin nuclei are present, and even tin patches not in contact with the surface of the particle can be seen (figure 4.15b). As growth rate decreases exponentially with temperature, the likelihood of more nucleation events taking place simultaneously increases, causing this distinct morphology.

The XRD pattern of these particles (figure 4.10) is similar to that of Lamellar particles with two minor differences. The metastable phase peak at 29° is much less intense in comparison, while the other metastable phase peaks can't be observed at

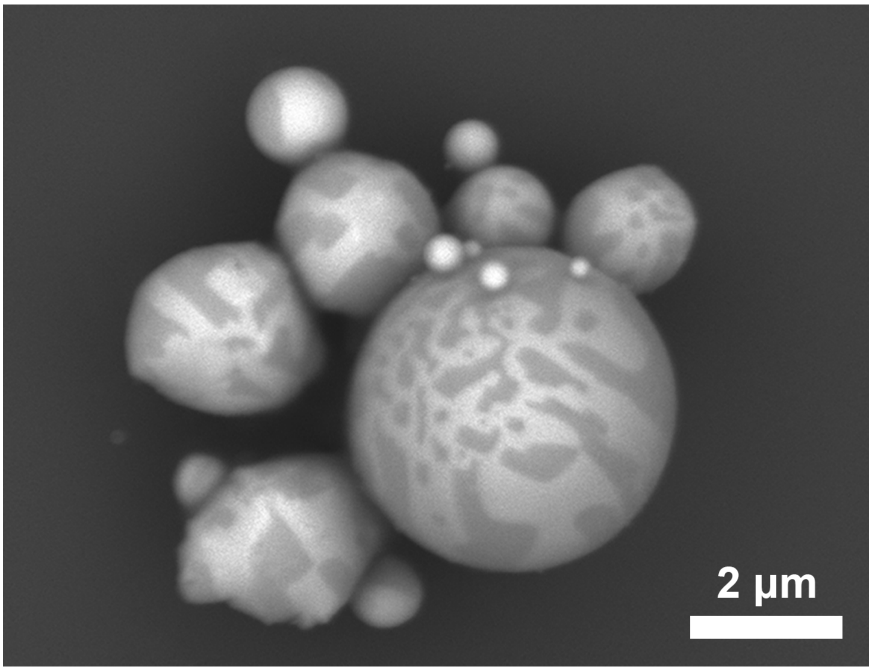

Figure 4.14: BSE-SEM micrograph of Composite Particles

all. Holding the particles at 160°C results in decomposition of the metastable phase. The equilibrium phase peaks are also broader, with larger full with half maximum values in comparison to Lamellar particles' peaks, seen in the equilibrium tin peaks at 31° and 32°, as well as the equilibrium bismuth peaks at 38° and 40°. The broader peaks indicate that the average crystallite size is lower according to Scherrer Equation [84], further proving that more nucleation events took place.

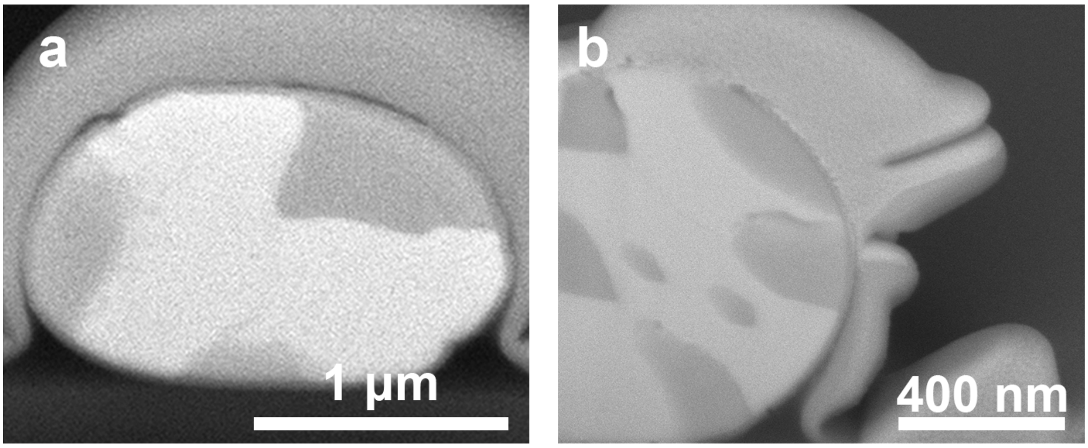

Figure 4.15: BSE-SEM micrographs of Composite particles' cores, milled using FIB

The control of undercooling of eutectic bismuth-tin particles by isolation of catalytic sites allows for their solidification with very high nucleation rates in comparison to their growth rates, allowing for the formation of new nuclei surpassing the growth of the already nucleated solid phases, making it possible to achieve very fine phase distributions. A schematic representation of the differing solidification kinetics, and the resulting morphologies is presented in figure 4.16.

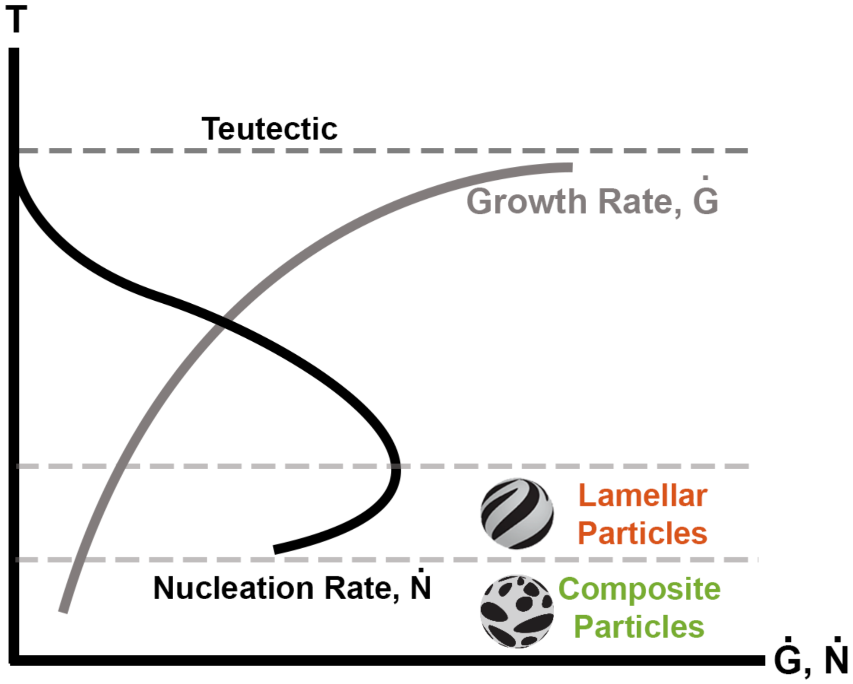

Figure 4.16: Schematic representation of the nucleation and growth rates of the Lamellar and Composite particles

The increase in fineness of the different phase regions also corresponds to increasing inter-facial area between the phases inside the particles. Defects are known to increase the performance of catalysts by acting as active sites for chemical reactions [85]. One possible application for the particles solidified with high undercooling is thus catalysis, as this characteristic makes them more efficient than their pure counterparts [74], and allows for a new parameter to be modified in order to increase the catalytic activity of particles besides composition or material type.

# CHAPTER 5

# LOW UNDERCOOLING MORPHOLOGIES

## 5.1 Janus Particles

Undercooling and solidification behavior can be controlled by intentional introduction of catalytic sites to the particles to promote solidification at a higher temperature, instead of removing nucleants or increasing cooling rate. Particles with different morphologies can be obtained this way, as it is clear that there is a correlation between the degree of undercooling upon solidification and the resultant morphology. Besides the previously discussed intentional modification of nucleation behavior, the effect of oxygen on nucleation catalysis of metals is also known. Studies on undercooling phenomena involve inert atmosphere to prevent this [33]. In line with this, the previously solidified Lamellar particles were heated up to 160°C in oxygen atmosphere, and cooled back to room temperature slowly with 2.5°C/min, with the resulting morphology being Janus Particles (figure 5.1a). This morphology is consistent across the entire batch of particles treated this way, with most of them displaying the Janus morphology (figure 5.1b).

This process is applied in DSC with 2.5°C/min, both in open atmosphere and inert atmosphere (figure 5.2). After metastable phase decomposition and melting, in nitrogen atmosphere, a comparatively less intense normalized peak is observed with an onset of 86°C, similar to the one in figure 4.12. The metastable decomposition peak is much less intense in comparison to the melting peak for this sample. This is attributed to the chaotic nature of DET, and the low amount of metastable phase once again has no bearing on the morphology obtained after subsequent processes. These particles, when observed under BSE-SEM, were mostly in the liquid phase. However,

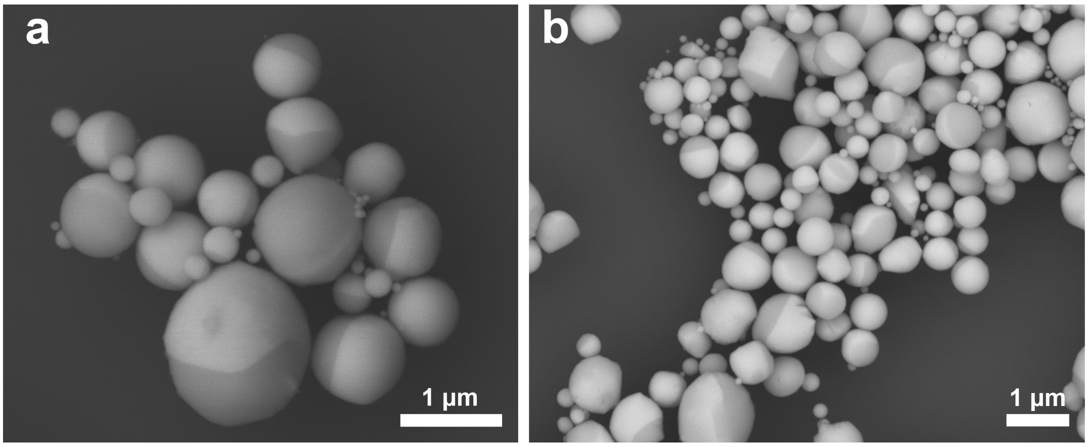

Figure 5.1: a,b) BSE-SEM micrograph of Janus particles

for the experiment repeated under open atmosphere, a more intense peak is observed at the same temperature. Once exposed to open atmosphere at high temperature , the particles will solidify with the Janus morphology whether they melt in inert or open atmosphere.

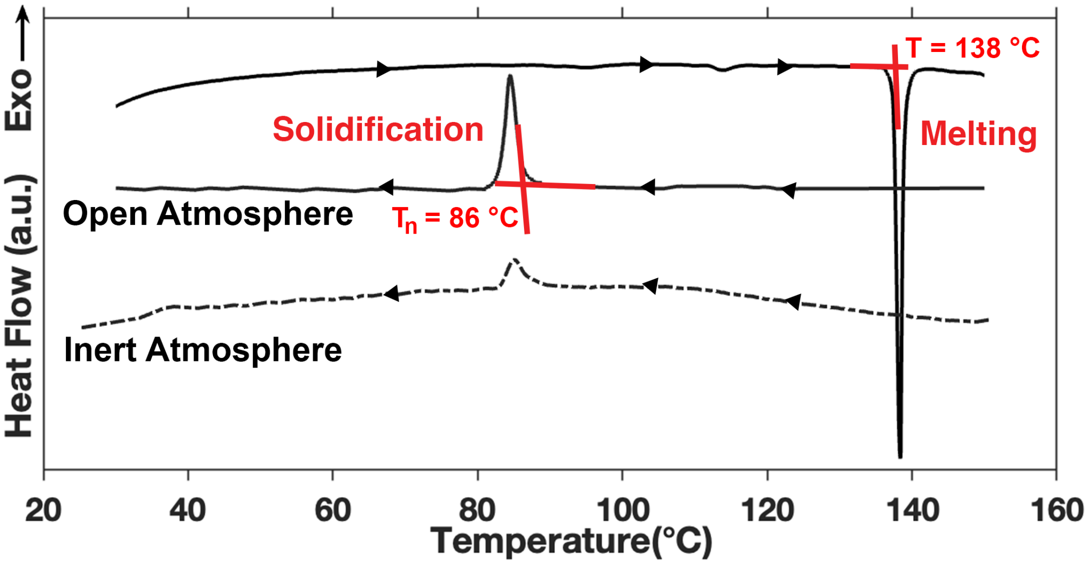

Figure 5.2: DSC analysis of the melting and high-catalytic potency site initiated solidification of eutectic BiSn particles, performed under inert nitrogen atmosphere and open atmosphere

Introduction of catalytic sites to a system and their subsequent purging has been investigated by Wilde et al. by using a 2 millimeter diameter gold droplet encased in glass [86]. They reported that successive cycles under inert atmosphere would increase the degree of undercooling of the droplet at each solidification event, but any instance of introduction of oxygen would drastically decrease this value. The proposed mechanism is that the oxide catalytic sites present in the droplet are accumulated at the solidifying front and diffuse into the glass, which acts as a flux. Introduced oxygen, on the other hand, reacts with dormant impurities inside the melt, activating them as catalytic sites and increasing the nucleation temperature. Even small increases in ppm-levels of oxygen significantly affects the solidification behavior of glass forming alloys [87].

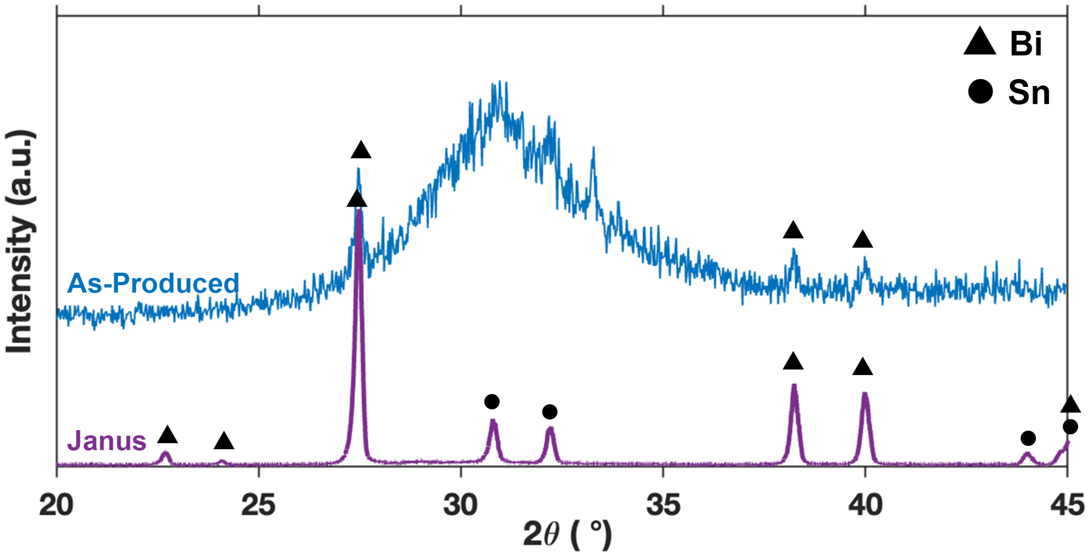

Figure 5.3: XRD pattern of Janus particles showing bismuth (PDF 04-006-7762) and tin (PDF 04-008-4977) peaks

When the mostly liquid batch of particles is solidified, the noise due to the amorphous phase disappears, as seen in the XRD pattern (figure 5.3). The metastable phase decomposes during the melting process, and cooled slowly, the particles solidify as the equilibrium phases, consistent with the BSE-SEM micrographs where two distinct contrasts are observed.

BSE-SEM micrographs of individual FIB-milled Janus particles reveal that once again, the phase distribution inside the particles' cores are consistent with their surfaces (figure 5.4). The Janus particles are in fact coreless, or compartmentalized particles, as opposed to patchy or core-shell. Upon closer inspection by contrast enhancement (figure 5.4b), traces of tin phase nuclei can be observed inside the bismuth region of

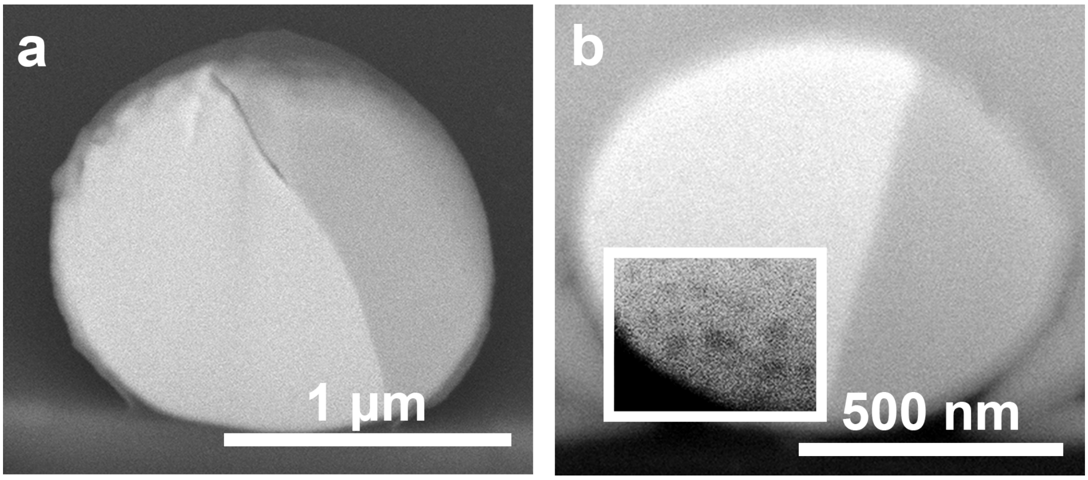

Figure 5.4: BSE-SEM micrographs of Janus particles' cores, milled using FIB

the particles. This finding reinforces the observation of Bhattacharya et al. regarding the solidification of eutectic bismuth-tin particles. They have shown, via in-situ XRD at high temperature, that for dispersions of eutectic bismuth-tin particles in contact with an aluminium matrix, bismuth is the phase which nucleates first, above the eutectic temperature, obtaining Janus particles embedded in aluminium matrix ([73]). Thermodynamically, the nucleation of both phases are equally favored for the eutectic composition. However, as the surface of the particles consists mostly of tin oxide, the composition of the liquid core shifts from the initial eutectic composition towards bismuth-rich, making it more favorable for bismuth to nucleate first. As such, it is concluded that the bismuth-rich region nucleates first, increasing the tin supersaturation in the liquid in front of the advancing solid phase, until the tin composition is high enough such that the tin-rich phase nucleates from the advancing front.

TEM analysis of the surface of nano-size solidified Janus particles confirms the existence of the previously mentioned oxide shell. A 3.5 nm oxide shell can be directly observed covering the particles. The coating is mostly amorphous, but nanocrystalline regions are also present (figure 5.5).

Because the catalytic site introduced has a higher catalytic potency according to equation 2.5, the energy barrier associated with nucleation is lower, and so solidification initiates at a higher temperature compared to solidification from the oxide shell. At higher temperature upon nucleation, nucleation rate is lower and growth rate, which decreases exponentially with temperature, is higher, compared to that of Lamellar particles. The introduction of catalytic sites promotes said high temperature nucleation, and as such, most of the particles solidify initiating from the site characterized by a 86°C DSC peak. Higher growth and lower nucleation rate results in more likelihood of each nuclei growing until completion of solidification, and increases the area of the two phase domains. Some variation is still observed among the particles, with a small amount deviating from the Janus morphology. As nucleation is a stochastic event, there is some randomness associated with it, but the particle morphologies are largely consistent (figure 5.1b).

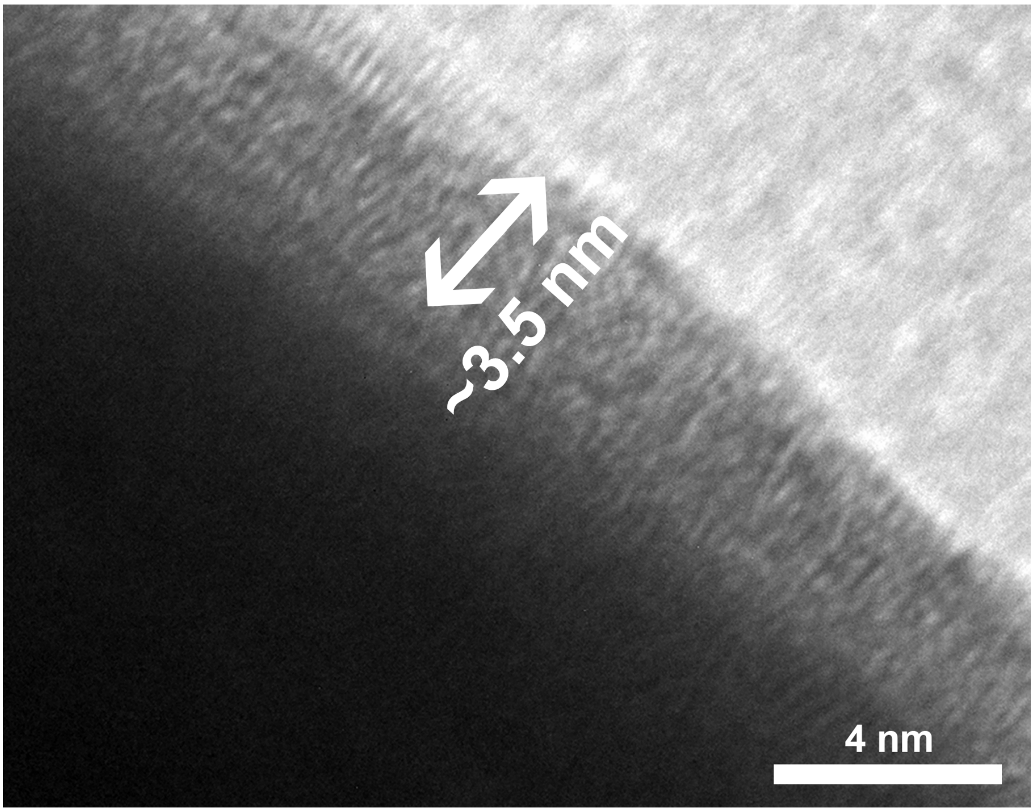

Figure 5.5: High Resolution TEM nanograph of the oxide shell of Janus particles

The processes applied on silicon wafers and DSC can also be extended to larger scales. DET can be used to produce undercooled particles in the gram scale, and as long as all particles are cooled and heated to the target temperatures, and are in contact with oxygen, they will solidify with the Janus morphology. As much as two grams of Janus particles have been produced with this two-step process, by particle production with DET and subsequent solidification and heat treatment using glass beakers as containers. As such, the method can be extended to produce Janus particles in the gram scale. For the first time in the literature, compartmentalized metallic Janus particles have been produced with a top-down method.

## 5.2 Triblock Janus Particles

Considering the relation between the oxide shell, oxygen content and nucleation, the influence of oxide layer on the nucleation event was investigated, with the aim to extend the library of phase distributions. It was reported in the literature that once tin nanoparticles are heated, a layer of SnO forms at temperatures below 400°C, with the rate being highest at 235°C [88]. Huh et al.[89] have stated that for bulk alloys of tin, the formation of a crystalline oxide towards the core of the particle will proceed inward at temperatures close to the melting point of tin, and the oxidation reaction is rate-limited by the diffusion of oxygen as the mobility of tin is high. As such, the as-produced particles were oxidized by heat treating them at 230° for 6 hours in open atmosphere. Upon furnace cooling with a rate of 2.5°/min to room temperature, such particles solidified with a Triblock Janus (Striped) phase distribution, with a tin-rich stripe on the center, and bismuth regions in the hemispheres, as seen in BSE-SEM micrographs (figure 5.6a). Although the center tin-rich stripe is observed in most particles, there is more variation in morphologies compared to Janus particles (figure 5.6b), possibly due to the difference in oxidation kinetics across them.

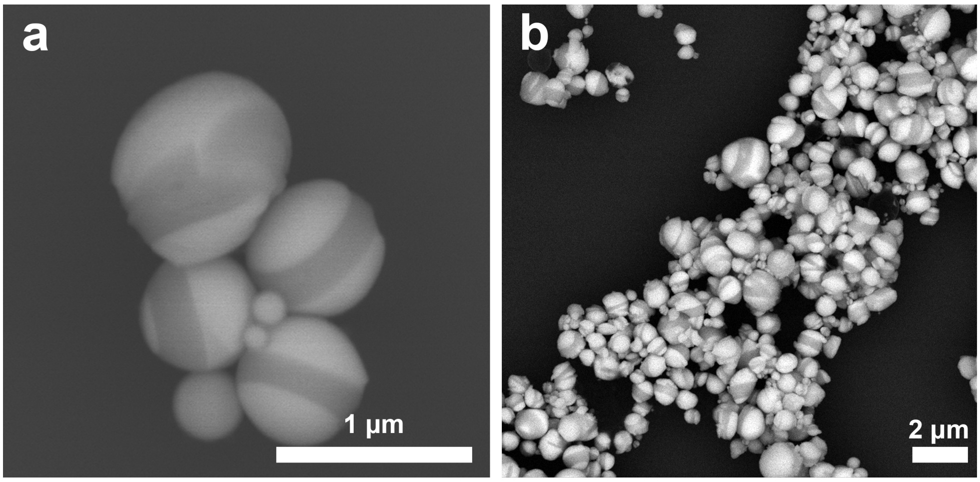

Figure 5.6: a,b) BSE-SEM micrographs of Striped particles

The XRD pattern of these particles exhibit no metastable peaks, but a fourth new phase appears, indexed to be stannous oxide (SnO), indicating the oxidation of particles to degrees observable in the XRD pattern, and further proving the nature of the oxide shell of the particles. Oxidation results in a notable shift in composition, evidenced by the significant reduction in the relative intensities of the pure tin-phase peaks (figure 5.7).

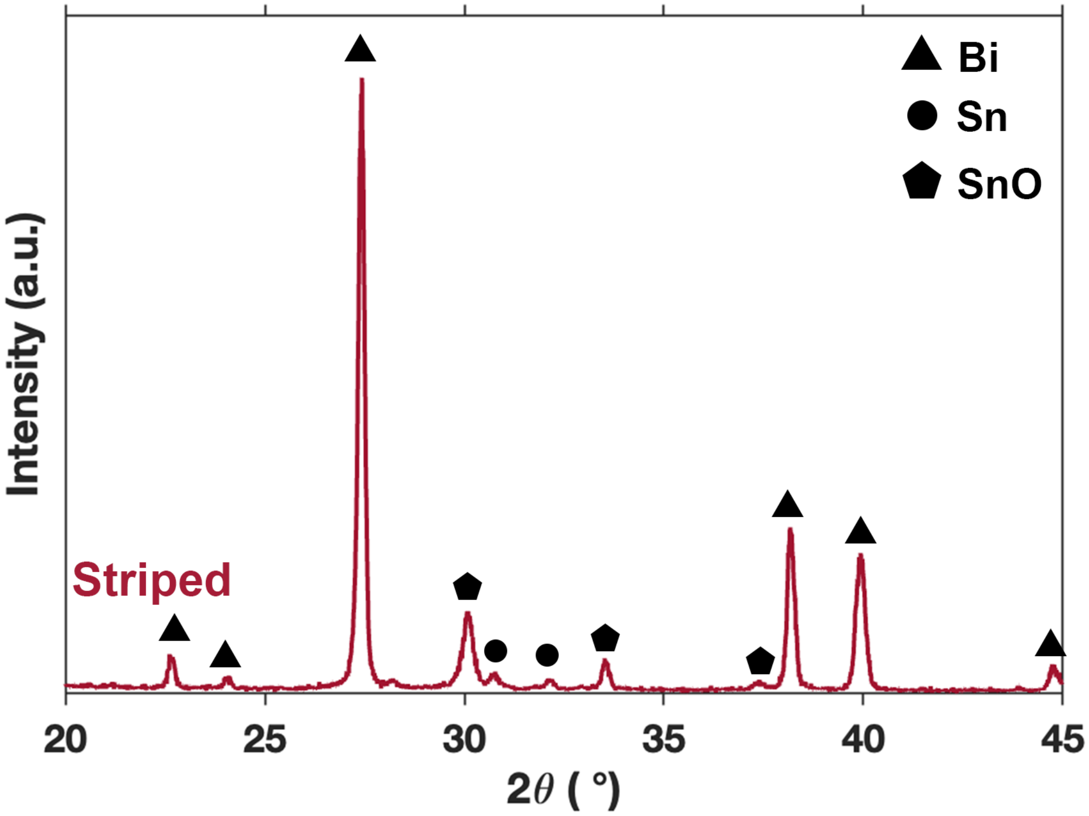

Figure 5.7: XRD pattern of Striped particles showing bismuth (PDF 04-006-7762), tin (PDF 04-008-4977) and tin oxide peaks (tin oxide peaks retrieved from [62])

TEM nanographs, presented in figure 5.8a, confirm this, with the oxide layer on the surface visibly thickening from 3 nm in Janus particles to 10 nm for particles oxidized in high temperatures.

A potential explanation for the morphology is the shift in composition of the particles. For equilibrium off-eutectic alloys rich in bismuth, the solidification temperature increases, with solidification initiating with primary-bismuth phase. This diffusion of bismuth to the solid nuclei from the liquid would result in a shift in the composi-

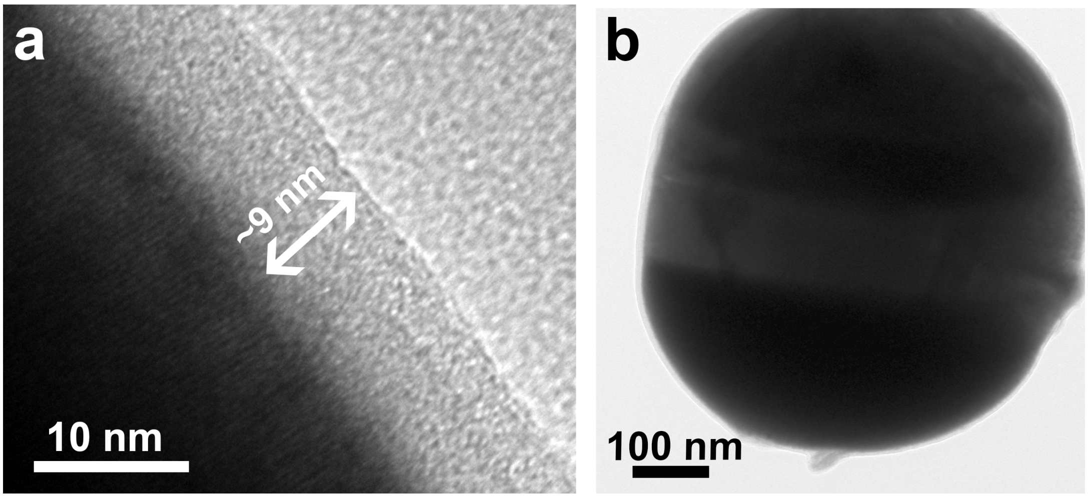

Figure 5.8: High resolution TEM nanographs of a) a Striped particle b) The oxide shell surrounding the particles

tion of the remaining liquid, bringing the liquids composition to the eutectic point, eventually resulting in eutectic solidification. The BSE-SEM micrograph of the core of Janus particle revealed the presence of tin nuclei in the bismuth-rich side (figure 5.4). It is expected that, after the solidification of the first bismuth hemisphere, the liquid is tin-rich enough so that the solidification of the tin-rich stripe initiates from this hemisphere. After the stripe solidifies, the liquid is bismuth-rich again so that the second hemisphere again solidifies as a bismuth rich region. From their HR-TEM nanographs, it is revealed that these particles are also coreless (figure 5.8b).

This treatment is strongly time dependant. When Janus particles are heated up to 230°C, and immediately heated back down to room temperature, they will solidify with the Janus morphology. Conversely, when Striped particles, which were already held at this temperature for 6 hours, undergo the same treatment, they will again solidify with Striped morphology. Once the thickness of the oxide shell increases by sufficient time spent at high temperature, the solidification behavior of the particles is permanently altered. These particles can also be produced in the gram scale with this treatment.

By intentional introduction of catalytic sites with high potency to the core-shell particle reactors, the solidification temperature is increased. At temperatures closer to the equilibrium solidification temperature, growth rate is higher relative to high undercooling solidification, as shown schematically in figure 5.9. As such, particles solidify with coarser structures, according to equation 2.3. While oxygen is known to activate dormant catalytic sites in particles, this property has been used to intentionally modify the undercooling behavior of the particles. Because the initial alloy is sufficiently pure, the particles produced from the alloy are uniform in their solidification characteristics. As such, applied large scale treatments have similar effects on their solidification characteristics. The relationship between the morphologies obtained and the solidification temperature at which they are observed is in strong agreement with the fundamental concepts of physical metallurgy, and can be used as a guideline to further predict and design particle structures.

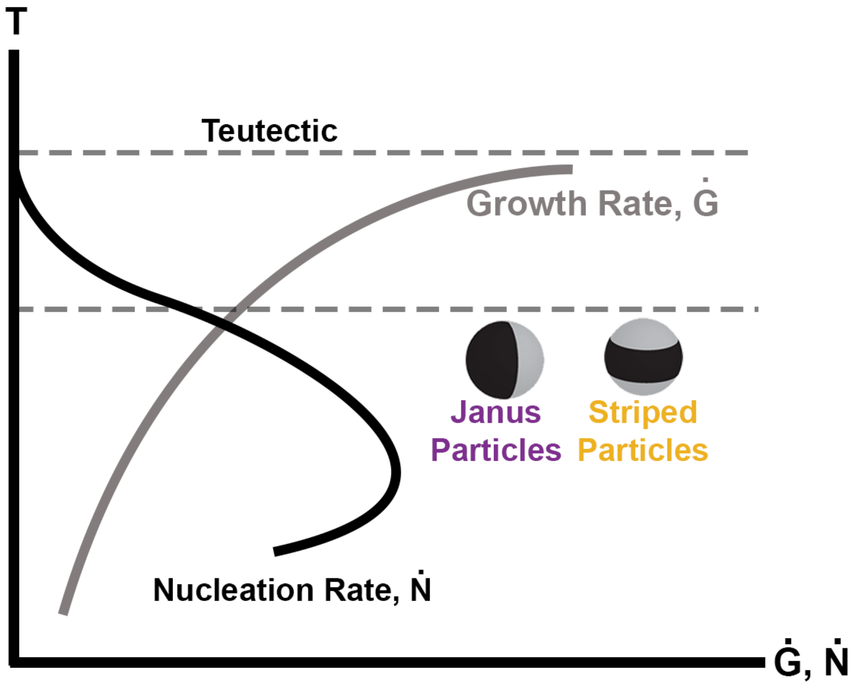

Figure 5.9: Schematic representation of the nucleation and growth rates of the Janus and Striped particles

# CHAPTER 6

# CONCLUSIONS AND FUTURE RECOMMENDATIONS

## 6.1 Conclusions

In this thesis, undercooled particles, which have been studied extensively to understand the various parameters affecting solidification, were used as a starting material to produce particles with various phase distributions. The relationship between the degree of undercooling, solidification kinetics and resultant morphologies were investigated.

Highly undercooled particles, stable in the liquid phase for more than three years, were produced using Droplet Emulsion Technique. The particles were thoroughly characterized structurally and thermally. The sub-zero temperature solidification of these particles without any modification, initiating from the nanometer-thick oxide shell on their surface, yielded particles with a complex regular eutectic structure with an inter-phase spacing in the order of nanometers. Further decreasing of their solidification temperature by quenching resulted in increase nucleation, as verified by investigation of the particles' cross sections, and a composite-like morphology with dispersions of tin-rich phase in a bismuth matrix.

The well known effect of oxygen concentration of the environment was used as a tool to introduce catalytic sites to the particles by taking the particles to high temperatures in an open air environment decreasing the degree of undercooling significantly. This decrease also resulted in a decrease in the nucleation rate, and the higher temperature allowed for more mobility and a faster growth rate of the phases. As a result of the increased solidification temperature, this resulted in a much coarser structure with the two equilibrium phases situated at the hemispheres of the particles, solidifying as the Janus morphology. The particles solidified in a coreless configuration, being homogeneous throughout their core to their surface. The production of particles with a structure normally restricted to bottom-up methods was made possible by this large scale processing technique.

The composition of the particles was modified by utilizing the surface oxide layer as another tool. High temperature processing of the particles resulted in further oxidation of the particles' surfaces, thickening the oxide layer and shifting the composition of the particles towards hypereutectic, as evidenced by direct imaging of the oxide layer using Transmission Electron Microscopy. This change of the oxide layer, in addition to shifting the composition, resulted in a modification of the solidification sequence of the particles. Another distinct and hard to produce morphology, Triblock Janus, was obtained as a result.

The underlying mechanisms for all of the described particle morphologies were found to be consistent with the fundamental concepts of solidification and physical metallurgy. These fundamentals were combined with the unconventional characteristics of sub-micron sized alloy particles. The particles were used as reactors for large scale control of microstructures, reducing the stochasticity associated with solidification in order to anticipate and control the resultant morphologies from solidification, and paving the way for more complex particle designs.

## 6.2 Future Recommendations

Particles produced with a process were found to share the same general features. However, there was some variation in particles sharing the same morphology. Janus particles produced had differing ratios of the volume of the two phases. The correlation between this variation and particle size, treatment parameters including time and temperature, and initial particle production steps should be investigated in order to find the underlying mechanism and increase the consistency in morphology of the particles. Another example is the variation in particle shape of striped particles, with many deviating from spheres.

Interrupted Differential Scanning Calorimetry, or in-situ observation of solidification can help improve understanding of the solidification mechanisms of the morphologies. Thus more accurate prediction of resultant morphologies from different treatments can be made. While ex-situ measurements allow for deductions to be made about nucleation and growth, it is clear that the phenomenon is much more complex and sensitive to unidentified parameters.

All the morphologies were obtained for the eutectic bismuth-tin system. For more understanding, more compositions of the same system should be studied to investigate the structures they would yield, as composition is one of the main factors in solidification sequence, and thus microstructure. Furthermore, different low melting point eutectic alloys should be studied to ensure applicability of the developed processes to other systems.

For all processes and characterizations in this thesis, particles with their as-produced size distribution were used. Segmentation of the particles into different size ranges would allow for correlations about microstructure and size to be drawn to see if any trend exists. As nanoparticles are also produced, and properties of materials change drastically in this range, separation of nanoparticles and subsequent property measurement is required for utilization of the particles in aforementioned applications.

# REFERENCES

[1] A. S. Pandit and H. K.D.H. Bhadeshia. Divorced pearlite in steels. *Proceedings of the Royal Society A: Mathematical, Physical and Engineering Sciences*, 468(2145):2767–2778, 2012.

[2] V. I. Izotov, V. A. Pozdnyakov, E. V. Luk'yanenko, O. Yu Usanova, and G. A. Filippov. Influence of the pearlite fineness on the mechanical properties, deformation behavior, and fracture characteristics of carbon steel. *Physics of Metals and Metallography*, 103(5):519–529, 2007.

[3] J. G. Byrne, M. E. Fine, and A. Kelly. Precipitate hardening in an Aluminium-Copper Alloy. *Philosophical Magazine*, 6(69):1119–1145, 1961.

[4] Juan Pedro Palomares-Baez, Emanuele Panizon, and Riccardo Ferrando. Nanoscale Effects on Phase Separation. *Nano Letters*, 17(9):5394–5401, 2017.

[5] J. Sun and S. L. Simon. The melting behavior of aluminum nanoparticles. *Thermochimica Acta*, 463(1-2):32–40, 2007.

[6] Kyung Jin Lee, Jaewon Yoon, and Joerg Lahann. Recent advances with anisotropic particles. *Current Opinion in Colloid and Interface Science*, 16(3):195–202, 2011.

[7] Jianzhong Du and Rachel K.O. Reilly. Anisotropic particles with patchy, multicompartment and Janus architectures: Preparation and application. *Chemical Society Reviews*, 40(5):2402–2416, 2011.

[8] Andreas Walther and Axel H.E. Müller. Janus particles: Synthesis, self-assembly, physical properties, and applications. *Chemical Reviews*, 113(7):5194–5261, 2013.

[9] Amar B. Pawar and Ilona Kretzschmar. Fabrication, assembly, and application of patchy particles. *Macromolecular Rapid Communications*, 31(2):150–168, 2010.

[10] Alla Synytska and Leonid Ionov. Stimuli-responsive Janus particles. *Particle and Particle Systems Characterization*, 30(11):922–930, 2013.

[11] Jaehyuck Choi, Yihua Zhao, Deying Zhang, Shu Chien, and Y. H. Lo. Patterned fluorescent particles as nanoprobes for the investigation of molecular interactions. *Nano Letters*, 3(8):995–1000, 2003.

[12] Nicole Glaser, Dave J. Adams, Alexander Böker, and Georg Krausch. Janus Particles at Liquid-Liquid Interfaces. *Langmuir*, 9780521848(22):5227–5229, 2006.

[13] Jonathan R. Howse, Richard A.L. Jones, Anthony J. Ryan, Tim Gough, Reza Vafabakhsh, and Ramin Golestanian. Self-Motile Colloidal Particles: From Directed Propulsion to Random Walk. *Physical Review Letters*, 99(4):8–11, 2007.

[14] Sharon C. Glotzer and Michael J. Solomon. Anisotropy of building blocks and their assembly into complex structures. *Nature Materials*, 6(8):557–562, 2007.

[15] Denis Rodríguez-Fernández and Luis M. Liz-Marzán. Metallic Janus and patchy particles. *Particle and Particle Systems Characterization*, 30(1):46–60, 2013.

[16] Andreas Walther and Axel H.E. Müller. Janus particles. *Soft Matter*, 4(4):663–668, 2008.

[17] J.H. Perepezko and J.S. Smith. Glass Formation and Crystallization in Highly Undercooled Te-Cu Alloys. 44:65–83, 1981.

[18] Debenedetti Pablo G. *Metastable Liquids: Concepts and Principles*. Princeton University Press, 1996.

[19] M Volmer and Weber. Keimbildung in übersättigten Gebilden. *Zeitschrift für Physikalische Chemie*, 119U(1):277–301, 1926.

[20] D. Turnbull and J. C. Fisher. Rate of nucleation in condensed systems. *The Journal of Chemical Physics*, 17(1):71–73, 1949.

[21] E R Buckle and Proc R Soc Lond A. Studies on the freezing of pure liquids - II. The kinetics of homogeneous nucleation in supercooled liquids. *Proceedings*

*of the Royal Society of London. Series A. Mathematical and Physical Sciences*, 261(1305):189–196, 1961.

[22] S. Karthika, T. K. Radhakrishnan, and P. Kalaichelvi. A Review of Classical and Nonclassical Nucleation Theories. *Crystal Growth and Design*, 16(11):6663–6681, 2016.

[23] K. F. Kelton, A. L. Greer, and C. V. Thompson. Transient nucleation in condensed systems. *The Journal of Chemical Physics*, 79(12):6261–6276, 1983.

[24] K. F. Kelton. *Crystal Nucleation in Liquids and Glasses*, volume 45. 1991.

[25] K F Kelton and A L Greer. *Nucleation in Condensed Matter Applications in*, volume Volume 15. 2010.

[26] David A. Porter, Kenneth E. Easterling, and Mohamed Y. Sherif. *Phase Transformations in Metals and Alloys*. Taylor & Francis Group, 3 edition, 2014.

[27] David Turnbull and Bernard Vonnegut. Nucleation Catalysis. *Industrial & Engineering Chemistry*, 44(6):1292–1298, 1952.

[28] John H. Perepezko. Nucleation in undercooled liquids. *Materials Science and Engineering*, 65(1):125–135, 1984.

[29] Yukang An, Lei Liang, Xiaolong Xu, Yuhong Zhao, and Hua Hou. Effect of bulk undercooling on microstructure transformation mechanism of rapidly solidified nickel alloys. *Journal of Materials Research and Technology*, 11:548–563, 2021.

[30] A. A. Burbelko, D. Gurgul, W. Kapturkiewicz, J. Poczatek, and M. Wrobel. Stochastic nature of the casting solidification displayed by micro-modelling and cellular automata method. *Solid State Phenomena*, 197:101–106, 2013.

[31] Giovanni Maria Maggioni and Marco Mazzotti. Modelling the stochastic behaviour of primary nucleation. *Faraday Discussions*, 179:359–382, 2015.

[32] D. M. Herlaeh, R. F. Cochrane, I. Egry, H. J. Fecht, and A. L. Greer. Containerless processing in the study of metallic melts and their solidification. *International Materials Reviews*, 38(6):273–347, 1993.

[33] D. Turnbull and R. E. Cech. Microscopic observation of the solidification of small metal droplets. *Journal of Applied Physics*, 21(8):804–810, 1950.

[34] Merton C. Flemings and Yuh Shiohara. Solidification of undercooled metals. *Materials Science and Engineering*, 65(1):157–170, 1984.

[35] JJ Richmond, JH Perepezko, SE LeBeau, and KP Cooper. In rapid solidification processing: Principles and technologies iii, ed. *R. Mehrabian*, 90, 1983.

[36] D. H. Rasmussen, K. Javed, M. Appleby, and R. Witowski. A procedure for the modification of undercooling of metal droplets. *Materials Letters*, 3(9-10):344–348, 1985.

[37] J H Perepezko and D R Allen. Initial crystallization reactions. 580:221–232, 2000.

[38] J. H. Perepezko and G. Wilde. Melt undercooling and nucleation kinetics. *Current Opinion in Solid State and Materials Science*, 20(1):3–12, 2016.

[39] M. G. Chu, Y. Shiohara, and M. C. Flemings. Solidification of highly undercooled Sn-Pb alloy droplets. *Metallurgical transactions. A, Physical metallurgy and materials science*, 15 A(7):1303–1310, 1984.

[40] Seema, Gyanender Kumar, Arun Sharma, Sanjay Kashyap, Zaidi Beddiaf, and Chander Shekhar. Thermodynamic modeling of Al–Si nanoalloy phase diagram. *Journal of Nanoparticle Research*, 23(11):1–9, 2021.

[41] Mohammad Amin Jabbareh and Fatemeh Monji. Thermodynamic modeling of Ag – Cu nanoalloy phase diagram. *Calphad: Computer Coupling of Phase Diagrams and Thermochemistry*, 60(October 2017):208–213, 2018.

[42] C. L. Chen, J. G. Lee, K. Arakawa, and H. Mori. Comparative study on size dependence of melting temperatures of pure metal and alloy nanoparticles. *Applied Physics Letters*, 99(1):97–100, 2011.

[43] G. L. Allen, R. A. Bayles, W. W. Gile, and W. A. Jesser. Small particle melting of pure metals. *Thin Solid Films*, 144(2):297–308, 1986.

[44] Y. L. Gao, E. Zhuravlev, C. D. Zou, B. Yang, Q. J. Zhai, and C. Schick. Calorimetric measurements of undercooling in single micron sized SnAgCu particles in a wide range of cooling rates. *Thermochimica Acta*, 482(1-2):1–7, 2009.

[45] Simge Çinar, Ian D. Tevis, Jiahao Chen, and Martin Thuo. Mechanical Fracturing of Core-Shell Undercooled Metal Particles for Heat-Free Soldering. *Scientific Reports*, 6(September 2015), 2016.

[46] Vesselin N. Paunov and Olivier J. Cayre. Supraparticles and "janus" particles fabricated by replication of particle monolayers at liquid surfaces using a gel trapping technique. *Advanced Materials*, 16(9-10):788–791, 2004.

[47] Liang Hong, Shan Jiang, and Steve Granick. Simple method to produce janus colloidal particles in large quantity. *Langmuir*, 22(23):9495–9499, 2006.

[48] Kyung Ho Roh, David C. Martin, and Joerg Lahann. Biphasic Janus particles with nanoscale anisotropy. *Nature Materials*, 4(10):759–763, 2005.

[49] Qian Chen, Sung Chul Bae, and Steve Granick. Directed self-assembly of a colloidal kagome lattice. *Nature*, 469(7330):381–384, 2011.

[50] Chien Chih Lin, Chu Wei Liao, Yi Cheng Chao, and Changshu Kuo. Fabrication and characterization of asymmetric Janus and ternary particles. *ACS Applied Materials and Interfaces*, 2(11):3185–3191, 2010.

[51] Jie Zhang, Bartosz A. Grzybowski, and Steve Granick. Janus Particle Synthesis, Assembly, and Application. *Langmuir*, 33(28):6964–6977, 2017.

[52] Stoyan K. Smoukov, Sumit Gangwal, Manuel Marquez, and Orlin D. Velev. Reconfigurable responsive structures assembled from magnetic Janus particles. *Soft Matter*, 5(6):1285–1292, 2009.

[53] Walter F. Paxton, Paul T. Baker, Timothy R. Kline, Yang Wang, Thomas E. Mallouk, and Ayusman Sen. Catalytically induced electrokinetics for motors and micropumps. *Journal of the American Chemical Society*, 128(46):14881–14888, 2006.

[54] Qingjia Chi, Zhen Wang, Feifei Tian, Ji'an You, and Shuang Xu. A review of fast bubble-driven micromotors powered by biocompatible fuel: Low-concentration fuel, bioactive fluid and enzyme. *Micromachines*, 9(10), 2018.

[55] Dhruv P. Singh, Udit Choudhury, Peer Fischer, and Andrew G. Mark. Non-Equilibrium Assembly of Light-Activated Colloidal Mixtures. *Advanced Materials*, 29(32):1–7, 2017.

[56] Laurent Bouffier, Valérie Ravaine, Neso Sojic, and Alexander Kuhn. Electric fields for generating unconventional motion of small objects. *Current Opinion in Colloid and Interface Science*, 21:57–64, 2016.

[57] Xiang Zhong Chen, Marcus Hoop, Fajer Mushtaq, Erdem Siringil, Chengzhi Hu, Bradley J. Nelson, and Salvador Pané. Recent developments in magnetically driven micro- and nanorobots. *Applied Materials Today*, 9:37–48, 2017.

[58] Xi Chen, Chao Zhou, and Wei Wang. Colloidal Motors 101: A Beginner's Guide to Colloidal Motor Research. *Chemistry - An Asian Journal*, 14(14):2388–2405, 2019.

[59] Shankar Balasubramanian, Daniel Kagan, Kalayil Manian Manesh, Percy Calvo-Marzal, Gerd Uwe Flechsig, and Joseph Wang. Thermal modulation of nanomotor movement. *Small*, 5(13):1569–1574, 2009.

[60] Yuan Gao and Yan Yu. How half-coated janus particles enter cells. *Journal of the American Chemical Society*, 135(51):19091–19094, 2013.

[61] Harry Seltz and F. J. Dunkerley. A Thermodynamic Study of the Tin-Bismuth System. *Journal of the American Chemical Society*, 64(6):1392–1395, 1942.

[62] W. J. Moore and L. Pauling. The Crystal Structures of the Tetragonal Monoxides of Lead, Tin, Palladium, and Platinum. 63:1392–1394, 1941.

[63] Lawrence E. Felton, Christopher H. Raeder, and David B. Knorr. The properties of tin-bismuth alloy solders. *Jom*, 45(7):28–32, 1993.

[64] Petr Vesely, Karel Dusek, and Angelika Stankova. Evaluation of Bismuth/Tin Solder Intermetallic Layers Based on Heating Factor. *Proceedings of the International Spring Seminar on Electronics Technology*, 2019-May:1–6, 2019.

[65] Shiqi Zhou, Chih han Yang, Shih kang Lin, Abdulaziz N. AlHazaa, Omid Mokhtari, Xiangdong Liu, and Hiroshi Nishikawa. Effects of Ti addition on the microstructure, mechanical properties and electrical resistivity of eutectic Sn58Bi alloy. *Materials Science and Engineering A*, 744(December 2018):560–569, 2019.

[66] J. L.Freer Goldstein and J. W. Morris. Microstructural development of eutectic Bi-Sn and eutectic In-Sn during high temperature deformation. *Journal of Electronic Materials*, 23(5):477–486, 1994.

[67] John D. Verhoeven. Fundamentals of physical metallurgy, 1975.

[68] Bismarck Luiz Silva, Guillaume Reinhart, Henri Nguyen-Thi, Nathalie Mangelinck-Noël, Amauri Garcia, and José Eduardo Spinelli. Microstructural development and mechanical properties of a near-eutectic directionally solidified Sn-Bi solder alloy. *Materials Characterization*, 107:43–53, 2015.

[69] Hiroaki Okamoto. *Desk handbook: phase diagrams for binary alloys*. ASM international, 2000.

[70] Martina Pilloni, Guido Ennas, Valentina Cabras, Valeria Denotti, Vijay Bhooshan Kumar, Anna Musinu, Zeev Porat, Alessandra Scano, and Aharon Gedanken. Thermal and structural characterization of ultrasonicated Bi-Sn alloy in the eutectic composition. *Journal of Thermal Analysis and Calorimetry*, 120(3):1543–1551, 2015.

[71] B.D. Cullity and S.R. Stock. *Elements of X-Ray Diffraction*. Pearson, 3 edition, 2014.

[72] W. Yoon and J. H. Perepezko. The effect of pressure on metastable phase formation in the undercooled Bi-Sn system. *Journal of Materials Science*, 23(12):4300–4306, 1988.

[73] Victoria Bhattacharya, E. Yamasue, K. N. Ishihara, and K. Chattopadhyay. On the origin and stability of the metastable phase in rapidly solidified Sn-Bi alloy particles embedded in Al matrix. *Acta Materialia*, 53(17):4593–4603, 2005.

[74] Jianbo Tang, Rahman Daiyan, Mohammad B. Ghasemian, Shuhada A. Idrus-Saidi, Ali Zavabeti, Torben Daeneke, Jiong Yang, Pramod Koshy, Soshan

Cheong, Richard D. Tilley, Richard B. Kaner, Rose Amal, and Kourosh Kalantar-Zadeh. Advantages of eutectic alloys for creating catalysts in the realm of nanotechnology-enabled metallurgy. *Nature Communications*, 10(1):1–14, 2019.

[75] Shuhada A. Idrus-Saidi, Jianbo Tang, Mohammad B. Ghasemian, Jiong Yang, Jialuo Han, Nitu Syed, Torben Daeneke, Roozbeh Abbasi, Pramod Koshy, Anthony P. O'Mullane, and Kourosh Kalantar-Zadeh. Liquid metal core-shell structures functionalised via mechanical agitation: The example of Field's metal. *Journal of Materials Chemistry A*, 7(30):17876–17887, 2019.

[76] Tingbiao Yuan, Zheng Hu, Yuxin Zhao, Jinjie Fang, Jun Lv, Qinghua Zhang, Zhongbin Zhuang, Lin Gu, and Shi Hu. Two-Dimensional Amorphous SnOx from Liquid Metal: Mass Production, Phase Transfer, and Electrocatalytic CO2 Reduction toward Formic Acid. *Nano Letters*, 20(4):2916–2922, 2020.

[77] Weilie Zhou, Robert P Apkarian, and Zhong Lin Wang. Fundamentals of Scanning Electron Microscopy. 2007.

[78] Dieter M. Herlach. Non-equilibrium solidification of undercooled metallic melts. *Metals*, 4(2):196–234, 2014.

[79] Ian D. Tevis, Lucas B. Newcomb, and Martin Thuo. Synthesis of liquid core-shell particles and solid patchy multicomponent particles by shearing liquids into complex particles (SLICE). *Langmuir*, 30(47):14308–14313, 2014.

[80] X. J. Han and B. Wei. Microstructural characteristics of Ni-Sb eutectic alloys under substantial undercooling and containerless solidification conditions. *Metallurgical and Materials Transactions A: Physical Metallurgy and Materials Science*, 33(4):1221–1228, 2002.

[81] Funsho K Ojebuoboh. Bismuth—Production, properties, and applications. *JOM*, 44(4):46–49, 1992.

[82] J. H. Perepezko, J. L. Sebright, P. G. Höckel, and G. Wilde. Undercooling and solidification of atomized liquid droplets. *Materials Science and Engineering A*, 326(1):144–153, 2002.

[83] Q. J. Zhai, Y. L. Gao, W. B. Guan, and K. D. Xu. Role of size and cooling rate in quenched droplet of Snsingle bondBi eutectic alloy. *Materials Science and Engineering A*, 441(1-2):278–281, 2006.

[84] Uwe Holzwarth and Neil Gibson. The Scherrer equation versus the 'Debye-Scherrer equation'. *Nature Nanotechnology*, 6(9):534, 2011.

[85] Fangyi Cheng, Tianran Zhang, Yi Zhang, Jing Du, Xiaopeng Han, and Jun Chen. Enhancing electrocatalytic oxygen reduction on MnO2 with vacancies. *Angewandte Chemie - International Edition*, 52(9):2474–2477, 2013.

[86] G. Wilde, J. L. Sebright, and J. H. Perepezko. Bulk liquid undercooling and nucleation in gold. *Acta Materialia*, 54(18):4759–4769, 2006.

[87] X.H. Lin, W. L. Johnson, and W.K. Rhim. Effect of Oxygen Impurity on Crystallization of an Undercooled Bulk Glass Forming Zr-Ti-Cu-Ni-Al Alloy. *Materials Transactions*, 38:473–477, 1997.

[88] Pengxiang Song and Dongsheng Wen. Experimental investigation of the oxidation of tin nanoparticles. *Journal of Physical Chemistry C*, 113(31):13470–13476, 2009.

[89] Moo Young Huh, Sun Ho Kim, Jae Pyoung Ahn, Jong Ku Park, and Byoung Kee Kim. Oxidation of nanophase tin particles. *Nanostructured Materials*, 11(2):211–220, 1999.

[90] Stephen Guattery and Gary L Miller. Downloaded 08 / 07 / 14 to 130 . 56 . 90 . 242 . Redistribution subject to SIAM license or copyright ; see http://www.siam.org/journals/ojsa.php. 21(3):703–723, 2000.

[91] Sunil L. Bangare, Amruta Dubal, Pallavi S. Bangare, and S. T. Patil. Reviewing otsu's method for image thresholding. *International Journal of Applied Engineering Research*, 10(9):21777–21783, 2015.

[92] K. V. Nekrasov, D. A. Laptev, and D. P. Vetrov. Automatic determination of cell division rate using microscope images. *Pattern Recognition and Image Analysis*, 23(1):105–110, 2013.

[93] John R. Grace and Arian Ebneyamini. Connecting particle sphericity and circularity. *Particuology*, 54:1–4, 2021.

# APPENDIX A

# DIGITAL IMAGE SEGMENTATION

In order to quantify the information between particles' sizes, shapes and their morphologies, individual particles have been segmented from SEM Micrographs, which contain all of the aforementioned information. The process is illustrated on a micrograph in figure A.1a.

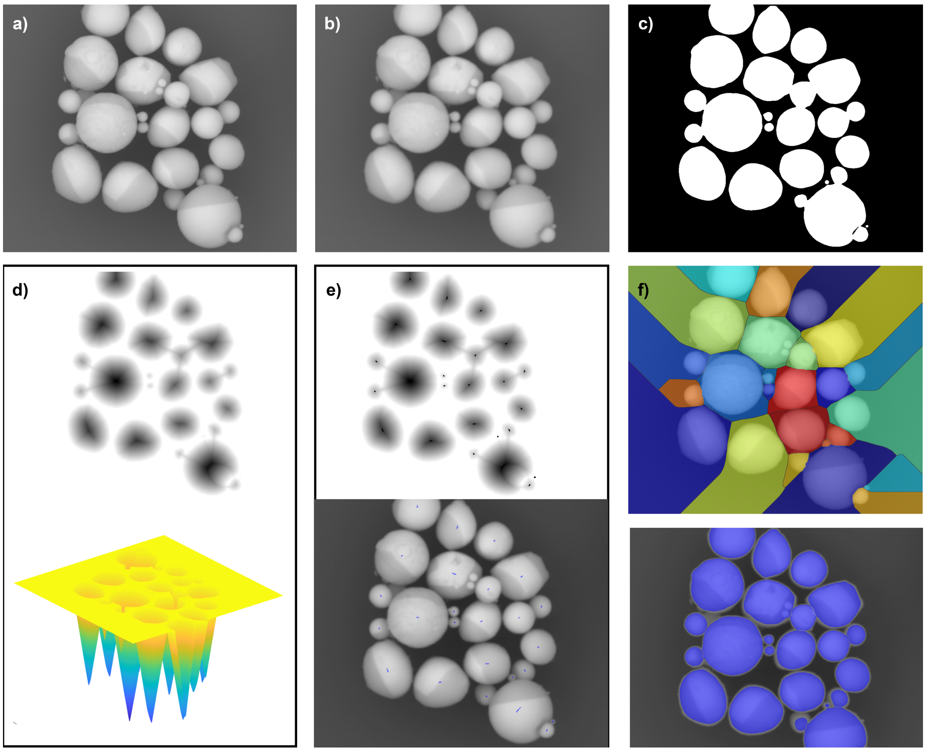

Figure A.1: The segmentation steps applied to SEM micrographs a) Initial Micrograph b) Gaussian filtered image c) Binarized image d) Euclidean distance transform, and its topological representation e) Particle locations found by extended minima trans- form, and marked on the original micrograph f) Particles segmented via watershed algorithm, and their locations marked on the original micrograph

Gaussian filter is first applied to the images to reduce noise, and prevent false positives in the thresholding step (figure A.1b) [90]. Otsu's method is applied to the filtered image in order to automatically determine the threshold value separating the background from the images [91], after which binarization is applied with the found value (figure A.1c). As the particles are mostly spherical, euclidean distance transform is used to locate the particles' centers, as usually only a single local minima is present as a result of this transformation for the micrographs [92]. The result of this transformation, and the resulting 3D surface of the image, is shown in figure A.1d. After distance transform is applied, local minima regions are extended to join adjacent local minima, preventing oversegmentation of individual particles, and forming the seeds which indicate individual particle locations (figure A.1e). Watershed transformation on the resultant image to locate the *ridges*, or the boundaries between the particles.

Once the boundaries are located, the individual particles are extracted from the micrograph, shown in figure A.2a. Particles are eliminated according to their sphericity, as the particles produced in this study are mostly spherical, or close to it, large deviations from sphericity result from faulty segmentation [93]. The sizes of the particles with sufficient sphericity were calculated by using the largest distance in the points comprising their perimeter (figure A.2).

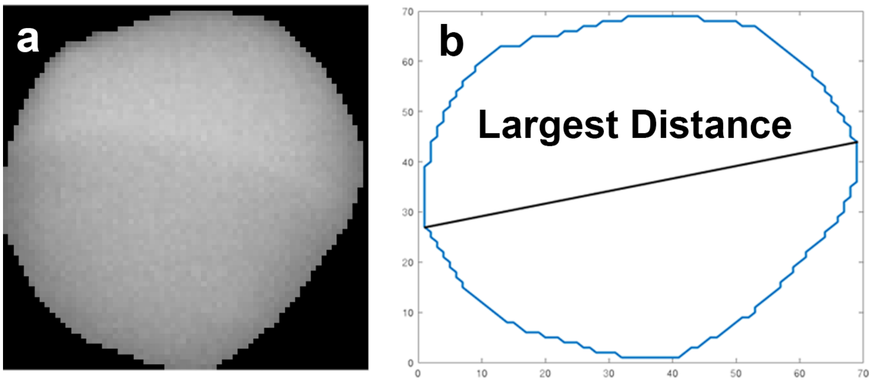

Figure A.2: a) An individual segmented particle b) Measured size of the particle